






Tumor and immune remodeling following radiotherapy in human renal cell carcinoma

Jacky Chow ¹, Adil Khan ¹, Madeline Gaudieri,¹ Brianna J Wasik,¹ Alexis Conway,² Kah Teong Soh,² Elizabeth A Repasky,¹ Thomas Schwaab,³ Paul K Wallace,² Scott I Abrams ¹, Anurag K Singh ⁴, Jason B Muhitch ¹

To cite: Chow J, Khan A, Gaudieri M, *et al.* Tumor and immune remodeling following radiotherapy in human renal cell carcinoma. *Journal for ImmunoTherapy of Cancer* 2023;11:e006392. doi:10.1136/jitc-2022-006392

► Additional supplemental material is published online only. To view, please visit the journal online (<http://dx.doi.org/10.1136/jitc-2022-006392>).

Accepted 03 April 2023



© Author(s) (or their employer(s)) 2023. Re-use permitted under CC BY-NC. No commercial re-use. See rights and permissions. Published by BMJ.

¹Department of Immunology, Roswell Park Comprehensive Cancer Center, Buffalo, New York, USA

²Department of Flow and Image Cytometry, Roswell Park Comprehensive Cancer Center, Buffalo, New York, USA

³Department of Urology, Roswell Park Comprehensive Cancer Center, Buffalo, New York, USA

⁴Department of Radiation Medicine, Roswell Park Comprehensive Cancer Center, Buffalo, New York, USA

Correspondence to

Dr Jason B Muhitch;
jason.muhitch@roswellpark.org

ABSTRACT

Background Studies evaluating peripheral patient samples show radiation can modulate immune responses, yet the biological changes in human tumors particularly at the cellular level remain largely unknown. Here, we address how radiation treatment shapes the immune compartment and interactions with cancer cells within renal cell carcinoma (RCC) patient tumors.

Methods To identify how radiation shaped the immune compartment and potential immune interactions with tumor cells we evaluated RCC tumors from patients treated only with nephrectomy or with radiation followed by nephrectomy. Spectral flow cytometry using a 35-marker panel was performed on cell suspensions to evaluate protein expression within immune subsets. To reveal how radiation alters programming of immune populations and interactions with tumor cells, we examined transcriptional changes by single-cell RNA sequencing (scRNAseq).

Results Spectral flow cytometry analysis revealed increased levels of early-activated as well as effector programmed cell death protein-1 (PD-1)⁺ CD8 T-cell subsets within irradiated tumors. Following quality control, scRNAseq of tumor samples from nephrectomy-only or radiation followed by nephrectomy-treated patients generated an atlas containing 34,626 total cells. Transcriptional analysis revealed increased transition from stem-like T-cell populations to effector T cells in irradiated tumors. Interferon (IFN) pathways, that are central to radiation-induced immunogenicity, were enriched in irradiated lymphoid, myeloid, and cancer cell populations. Focused cancer cell analysis showed enhanced antigen presentation and increased predicted TRAIL-mediated and IFN-mediated interactions between tumor cells and the same effector T-cell subsets increased by radiation. TRAIL and IFN pathways enriched in irradiated tumors were associated with survival in patients treated with immunotherapy.

Conclusions These findings identify the source of IFN enrichment within irradiated RCC and reveal heightened levels of PD-1⁺ CD8⁺ T-cell subsets and increased probability of interactions with tumor cells following standalone radiation treatment. This study provides a window into the irradiated tumor-immune microenvironment of patients and rationale for treatment combinations.

WHAT IS ALREADY KNOWN ON THIS TOPIC

⇒ Preclinical models have investigated mechanisms for immunostimulatory effects of radiation including vascular remodeling for immune cell infiltration, increased antigen expression, and immunogenic cell death. Certain clinical trials have leveraged these findings to show patient responses to combinations of radiation with immunotherapy, though overall results are mixed.

WHAT THIS STUDY ADDS

⇒ Due to the scarcity of on-treatment samples, few studies have examined irradiated human tumors. This limitation occludes the optimization of combination strategies with immunotherapy. Here, we provide compartment-specific analysis of renal cell carcinoma from patients treated with radiation to demonstrate enrichment of critical interferon pathways within immune and tumor cells. We find heightened levels of programmed cell death protein-1⁺ T-cell populations that include activated and exhausted subsets and increased predicted interferon-mediated interactions between these T-cell populations and tumor cells within irradiated patient tumors.

HOW THIS STUDY MIGHT AFFECT RESEARCH, PRACTICE OR POLICY

⇒ These findings offer a glimpse into the cell-specific effects of radiation within the human tumor micro-environment and provide rationale for trials that rely on intratumoral T-cell activity following radiotherapy for patient responses.

INTRODUCTION

The results of several encouraging clinical studies using radiation with immunotherapy^{1–4} have, in part, advanced the opening of over 400 trials that combine a spectrum of immune checkpoint blockade (ICB) and radiation strategies.^{5–7} Intense investigation of tumor samples from patients treated with standalone ICB or combinations of ICB with radiation has provided insight into the mechanisms of action^{8–9} and biomarkers

of response.¹⁰ Yet relatively few studies have examined tumors from patients treated with radiation alone. This gap regarding the isolated effects of radiotherapy in the patient tumor microenvironment obscures rationale towards optimal radiation and immunotherapy regimens.

Recent transcriptional analyses of in situ irradiated patient tumors have begun to shed light on the immunostimulatory effects of radiation.^{11–15} Findings showing a correlation between interferon (IFN) pathways within the primary tumor and responses at metastatic lesions following ICB treatment,¹¹ strengthen the importance of IFN pathways to CD8⁺ T cell-mediated effects following radiation as noted in preclinical reports.^{16, 17} However, bulk transcriptional investigation of samples containing pooled stromal, immune, and cancer cell material are unable to resolve the source of signals or relative contributions of each subset. As interest continues to grow regarding synergistic effects between radiation and immunotherapy, there remains a critical need to evaluate how radiotherapy impacts the tumor landscape in patients at the cellular level.

To assess the impact of radiation on the human tumor microenvironment with the resolution necessary for determining compartment-specific effects, we performed high-dimensional, 35-marker spectral flow cytometry of tumors from patients with renal cell carcinoma (RCC) treated with stereotactic body radiation therapy (SBRT). We found increased levels of early-activated as well as effector CD8⁺ T-cell subsets within irradiated tumors. To provide insight into how radiation remodels immune subsets and interactions with tumor cells, we performed single-cell RNA sequencing (scRNAseq). Across immune classes, we identified increased cell maturation and immunogenic signals from irradiated tumors. Among tumor cells, we observed heightened antigen expression, antigen presentation machinery, and enrichment of IFN pathways within irradiated tumors. Investigation of predicted interactions between effector CD8⁺ T cells and cancer cells in irradiated RCC revealed enhanced immune-effector expression signals that are associated with survival and response to immunotherapy of patients with RCC.

MATERIALS AND METHODS

Sample preparation

Specimens were dissociated into single-cell suspensions and frozen immediately upon procurement as described.¹³ All samples (see online supplemental table 1) processed for spectral flow cytometry or scRNAseq were thawed and analyzed on the same day.

Spectral flow cytometry

Single-cell suspensions were thawed then stained with titrated and saturating concentrations of antibodies listed in online supplemental table 2 using FOXP3/transcription factor staining kit (eBiosciences). Samples were acquired on a Cytex Aurora (Cytex Biosciences) flow cytometer (see online supplemental methods).

Analysis was performed using FCS Express 7 software package (De Novo Software, V.7.08.0018). A total of 11 patient samples (6 controls and 5 SBRT, online supplemental table 1) were analyzed for viability and homogeneity. Forty thousand randomly selected cells from each patient were concatenated to a single FCS file. The t-distributed stochastic neighbor embedding (t-SNE) plots were generated using CD45, CD3, CD4, CD8, CD11c, CD14, CD25, CD31, CD33, CD56, CD57, CD68, CD204 and CD261 to identify cell types. For CD8⁺ T-cell analysis, CD3⁺, CD8⁺ cells were extracted and then 10,000 randomly selected cells were concatenated from each patient. Prior to running t-SNE, unsupervised FlowSOM hierarchical clustering was performed using CCR4, CCR5, CCR6, CCR7, CD25, CD27, CD28, CD38, CD45-RA, CD45-RO, CD56, CD57, CD127, CXCR3, CX3CR1, HLA-DR, KI67, LAG3, PD-1, TIGIT, TIM3, and TOX to assign clusters to CD8⁺ T cells. Multiple cluster numbers were tested, and 15 clusters were chosen for final visualization as they best highlighted the differences in marker expression within subsets. All t-SNE analyses were run with a Barnes-Hut Approximation of 0.50 and a perplexity of 50. Analysis was run for 5,000 iterations. Cluster frequency plot was generated using GraphPad Prism software (V.9.1.2).

RNA sequencing

Samples were stained with LIVE/DEAD Fixable Aqua (Thermo Fisher cat. L34957) and flow sorted for at least 100,000 viable cells. Single-cell libraries were generated using the 10x Genomics 3' gene expression (V.3) kit. Samples were loaded into the Chromium Controller (10x Genomics) and partitioned into nanoliter-scale gel beads-in-emulsion with a single barcode per cell. Reverse transcription was performed, and the resulting complementary DNA was amplified. Gene expression libraries were generated and evaluated on D1000 screentape using a TapeStation 4200 (Agilent Technologies) and quantitated using Kapa Biosystems PCR quantitation kit for Illumina. They were then pooled, denatured, and diluted to 300pM with 1% PhiX control library added. The resulting pool was loaded into the NovaSeq Reagent cartridge and sequenced on a NovaSeq 6000 (Illumina).

Cell classification (RNA sequencing)

A representative cohort of SBRT samples was selected for scRNAseq based on bulk RNA data.¹³ Dimensional reductions were determined from the top 500 most variant genes. In all cases, dimensional reduction was calculated with data from all samples pooled together. Uniform Manifold Approximation and Projection (UMAP) and t-SNE coordinates were calculated independently. Each UMAP calculation included the first 50 principal components for a given analysis. Cell classification was made by calculating UMAP coordinates in scatter. The first level of categorization was assigned by expression of cell lineage markers in visually determined clusters. Lymphocyte classification was called based on *CD3D*, *CD3E*, *CD3G*, and *NKG7* expression, while myeloid cells were called based

on *CD68* and major histocompatibility complex (MHC)-II expression.

All subclustering was performed using UMAP coordinates as preserved global structure assisted in cluster identification; these are shown in online supplemental figures. Final visualization for main figures were shown using t-SNE coordinates to allow within-cluster resolution that was lost to UMAP compression. Localized gene expression reflects log-normalized counts calculated with *scater*. For each heatmap, cluster-wise gene expression is the z-score based on scaled log-normalized counts of the cell subset; expression was visualized using the *ComplexHeatmap* package. Where present, subclass composition was determined by first creating a new data set composed from a random sample of cells from each treatment group towards equal sizes and then comparing the balance within each subclass. Among the population of interest, the data set was first reduced to random subsamples of equal size from each treatment using the *sample* function in R. All χ^2 tests were performed in R on a 2×2 contingency table that distributed cells by treatment group and indicated subclass.

Differential gene expression analysis

Comparisons of cell populations were calculated between treatments. Zero-counts were dropped before any calculations. Differential gene expression (DGE) was calculated based on log2 counts per million normalized counts using the *scater* package. Calculations were performed using the *limma* R package with Benjamini-Hochberg correction. DGE was defined based on an absolute log2 fold change >1 with an adjusted p value <0.05. Pathway enrichment analysis was determined using the ranked-list methods in *ReactomePA*, *clusterProfiler*, and *fgsea*. Pathway enrichment significance was determined based on an adjusted p value <0.05.

Pseudotime analysis

Pseudotime analyses were performed with the *slingshot* package in R.¹⁸ Cell subsets were plotted according to recalculated UMAP coordinates using *scater*; lineages and curves were calculated in *slingshot*¹⁸; cell lineages by treatment group were visualized using the *ggplot2* package; smoothed gene expression of log-normalized counts across lineages and pseudotime was visualized also using *ggplot2*. Localized expression within the pseudotime UMAP plot was log-normalized counts. Similar to previous analysis for monocyte and macrophage projections,¹⁹ a small stray cluster was removed after subclustering. The pseudotime starting node was assigned by high density of cells from classical monocyte subclasses.

Cell interaction analysis

Ligand to receptor and target gene interaction prediction was performed using the *nichenetr* package (see online supplemental methods).²⁰ Plots were generated with *ComplexHeatmap*. Source and target cell annotation was determined as follows: average and percent

positive for log-normalized counts was calculated for each gene by treatment group and represented by color and size, respectively; DGE was calculated as described above to obtain log2 fold change as well as adjusted p values and were represented by color and size, respectively; expression level by subclass was determined by scaled log-normalized counts.

Analysis of public data sets

Survival analysis was based on data from The Cancer Genome Atlas (TCGA)-KIRC project. Data were retrieved by the *TCGAbiolinks* package with the following parameters: only tumors with bulk RNA data; STAR—Counts; primary tumors only; tumor stage I–III. IFN- γ score was determined by summing scaled expression of *IFNG* and *IFNGR1*; TRAIL score was determined by summing scaled expression of *TNFSF10* and *TNFRSF10A*. The score threshold for ‘hi’ was being among the top 70% for the given score; this put approximately 50% of samples into the IFN- γ hi TRAIL hi group. Kaplan-Meier curves, HRs, and significance were calculated using the *survival* and *survminer* packages. ICB response analysis was based on expression data provided from a trial that investigated angiogenesis blockade with ICB.²¹ The significance of pretreatment IFN- γ /TRAIL score, described above, to clinical response was determined by analysis of variance test in R. The significance of the score or expression levels of individual genes with respect to complete responders versus others was determined by two-tailed t-test.

RESULTS

Single-cell analysis of SBRT-treated RCC

To determine how radiation shapes immune populations in human tumors, we analyzed samples from a clinical trial (NCT01892930) (figure 1A), wherein patients received 15 Gy SBRT to the primary RCC lesion 4 weeks prior to nephrectomy. Details of the trial, patient sex, staging, and long-term survival have been described.^{13 22} All tumors and patient characteristics are listed in online supplemental table 1.

Nephrectomy tumors from patients with RCC who had no prior treatments (controls, n=6) and SBRT-treated tumors (n=5) were analyzed by high-dimensional spectral flow cytometry. Our prior studies revealed increased T-cell clonality and heightened levels of proliferating T cells in irradiated RCC.^{13 22} To determine how radiation impacted discrete immune subsets we designed a 35-marker antibody panel (online supplemental table 2) for deep profiling of lymphocyte subsets. Based on expression of hallmark markers, we identified broad immune and non-immune subsets (figure 1B–C, online supplemental table 3). Comparison between control and SBRT groups revealed distinct patterns in CD8⁺ T-cell populations (figure 1D, online supplemental figure 1A). Consistent with prior studies²² we found no difference in overall T-cell numbers (online supplemental figure 1A–C), suggesting that expression patterns or subset

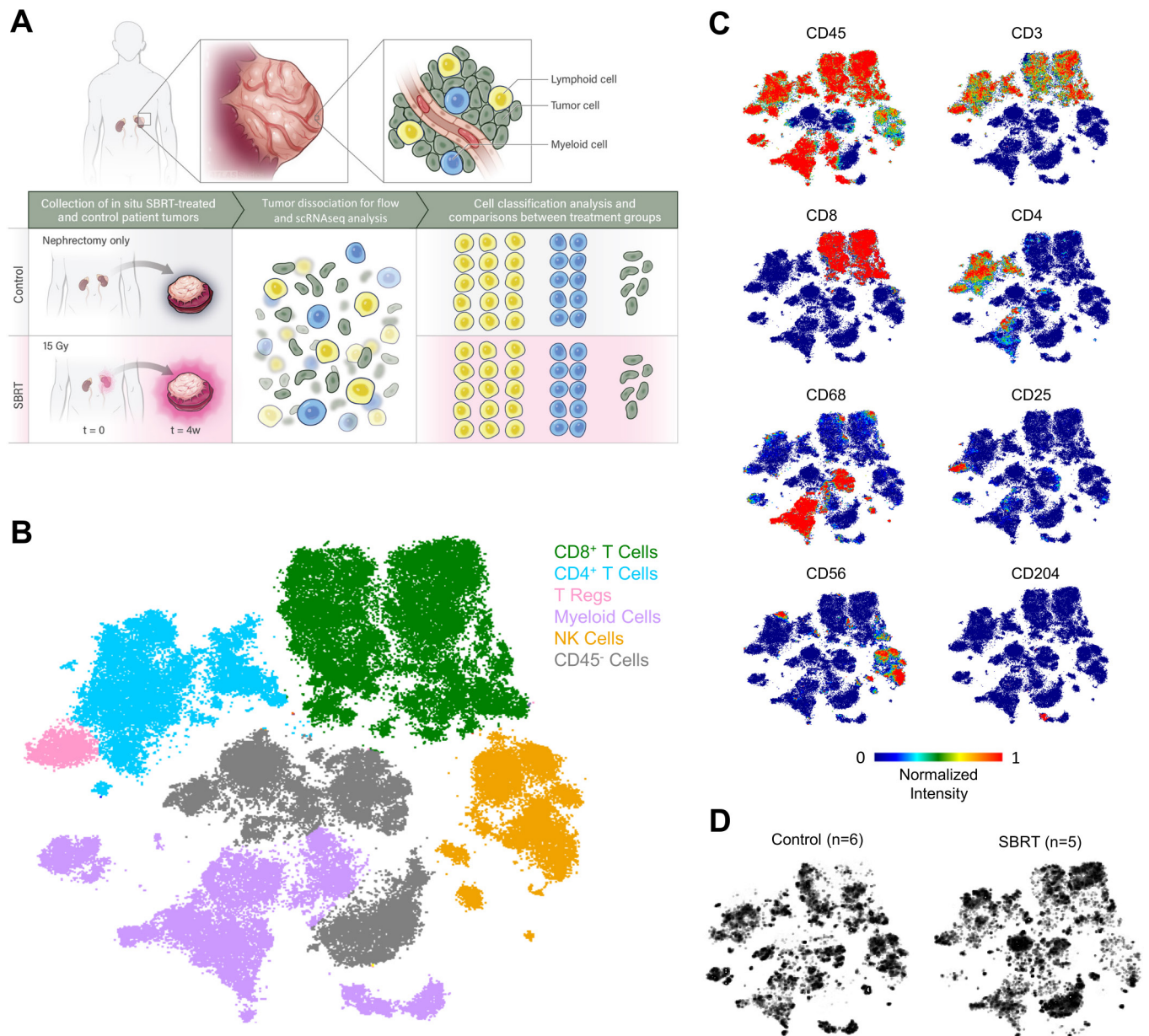


Figure 1 Single-cell analysis of renal cell carcinoma tumors following radiation therapy. (A) Schematic for determining cell-type specific effects of treatment by spectral flow cytometry and scRNAseq analysis of in situ radiated primary renal cell carcinoma tumors and nephrectomy-only control tumors. (B) t-SNE plot showing identified cell populations following spectral flow analysis performed on single-cell suspensions. Colors and labels correspond to broad, main cell classification. Individual t-SNE plots for indicated markers (C) and total cells within control (left) or SBRT-treated groups (right) (D). SBRT, stereotactic body radiation therapy; scRNAseq, single-cell RNA sequencing; t-SNE, t-distributed stochastic neighbor embedding.

composition was altered in SBRT-treated samples rather than overall CD8⁺ T-cell infiltration.

To determine if irradiated tumors were enriched for specific CD8⁺ T-cell subsets, we performed unsupervised hierarchical FlowSOM analysis (figure 2A, online supplemental figure 2A,B). Clusters were not dominated by T cells from a single patient (online supplemental figure 2C,D, online supplemental table 4). The expression of lymphocyte markers was used to characterize each identified subset (figure 2B, online supplemental figure 2E). Comparisons across samples identified four significantly enriched clusters in SBRT-treated tumors (figure 2C).

In line with prior immunohistochemistry (IHC) analysis, two of these clusters (cluster 14 and cluster 15) were programmed cell death protein-1 (PD-1)⁺ with high levels of CCR5 and Ki67 expression (figure 2D, online supplemental figure 3).²² PD-1^{int}, CCR5^{hi}, Ki67^{lo} cluster 12 was also increased in SBRT-RCC. SBRT-treated RCC had heightened levels of cluster 3 which expressed CD45RA at levels similar to a representative naïve-like T-cell subset (cluster 2, figure 2D) and low levels of PD-1 indicating enrichment of a less-activated T-cell subset.

These findings led us to perform a comprehensive analysis of the immune and tumor compartments through

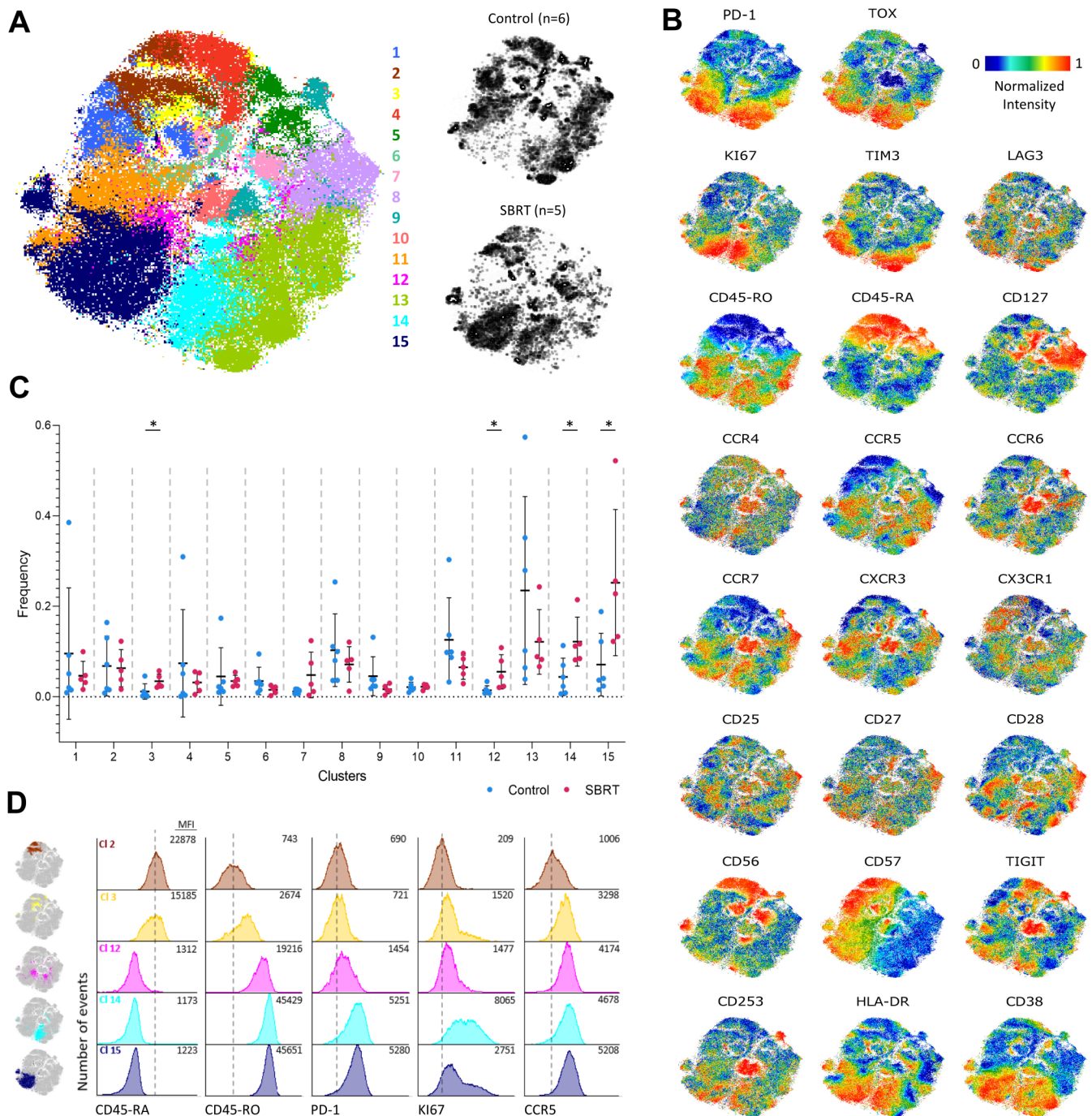


Figure 2 Analysis of CD8⁺ T cells by spectral flow cytometry. (A) t-SNE plot of CD8⁺ T cells analyzed by spectral flow analysis. Colors and labels correspond to broad CD8⁺ T-cell clusters identified by FlowSOM clustering (left). t-SNE plots (right) represent cells within control (top) or SBRT-treated groups (bottom). (B) Expression of indicated markers is displayed on individual t-SNE plots. (C) Frequency of cells in each of the 15 identified clusters within control (blue) and SBRT-treated (red) patient specimens. Statistical significance was calculated using multiple unpaired t-tests (* $p < 0.05$). Data presented as mean \pm SD. (D) Single parameter histograms are shown for expression comparisons across the four significantly different clusters (3, 12, 14, and 15) between control and SBRT group and a naïve-like T-cell representative cluster (2). Numbers indicate median fluorescent intensity (MFI) value. Vertical dashed lines indicate the MFI value for cluster 2. SBRT, stereotactic body radiation therapy; t-SNE, t-distributed stochastic neighbor embedding.

scRNAseq. Analysis initiated with unsupervised, graphical clustering of cells (figure 3A) from controls (n=2) and SBRT-treated tumors (n=4). High level classification was based on marker genes used in scRNAseq analysis of RCC and other malignancies.^{8 19 23 24} Following quality control,

the single-cell data set contained 34,626 total cells. 24,233 cells were identified as lymphocytes through the expression of genes including *CD3D*, *CD8A*, *CD4*, and *NKG7*; 7586 myeloid cells were based on expression of *CD68*, *APOE*, and *CLEC9A*; tumor cells were identified by *CA9*

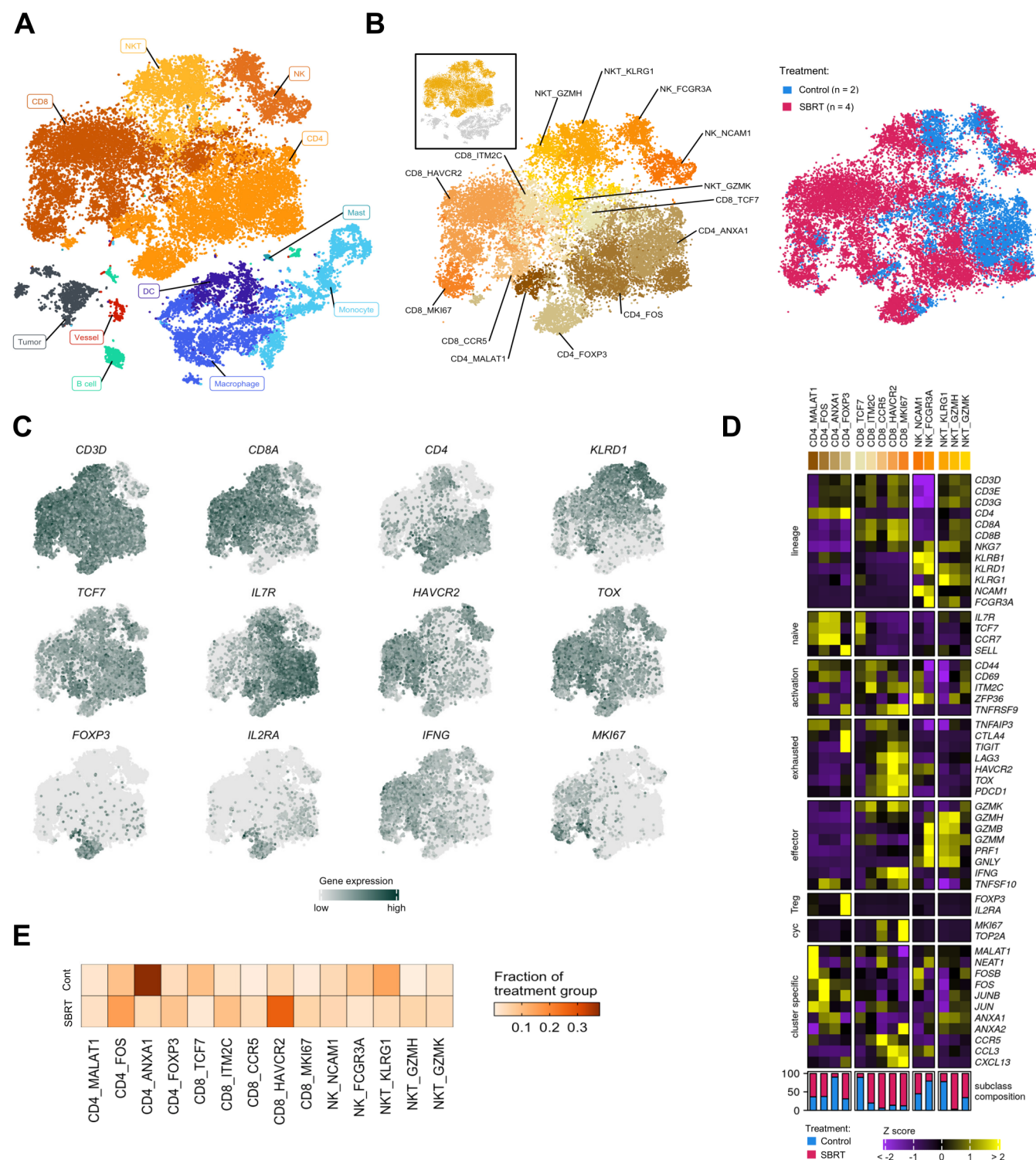


Figure 3 scRNAseq analysis of renal cell carcinoma following radiation therapy. (A) t-SNE of all cells analyzed for this study by scRNAseq. Colors and labels correspond to broad, main cell classification. (B) Distribution of lymphocytes shown as a subset from the t-SNE and by treatment group. Colors and labels correspond to cell subclassification (left) and treatment (right). Inset, showing cells subset from parent t-SNE for analysis. (C) Localized gene expression for indicated genes within the t-SNE. (D) Top, heatmap showing expression of genes used for lymphocyte subclassification. Bottom, bar graph showing subclass composition by treatment group after controlling for different total lymphocyte numbers between treatment groups. (E) Distribution of lymphocyte subclasses pooled within each treatment group. SBRT, stereotactic body radiation therapy; scRNAseq, single-cell RNA sequencing; t-SNE, t-distributed stochastic neighbor embedding.

and *NAT8* expression totaling 1590 cells (online supplemental figure 4A-D). Sparing numbers of mast, blood vessel, and B cells were similarly identified (online supplemental figure 4A,B). Between treatment groups, we identified 13,422 total cells from control tumors and 21,204 cells from SBRT-treated RCC. Previous bulk transcriptomic results detected heightened expression of *IFNG* and interleukin (*IL-16*) along with broad immunogenicity and IFN pathways in radiation-treated patient tumors.¹³ Analysis by scRNAseq mapped expression of these genes to specific cell types (online supplemental figure 4E).

Lymphocyte heterogeneity in radiated and treatment-naïve RCC

To evaluate the effect of in situ radiation on tumor-infiltrating natural killer (NK) and T cells, we first subset these for specific investigation (figure 3B). Isolated T lymphocytes and NK cells were reclustered (online supplemental figure 5A) before assigning a second level of categorization derived from expression of hallmark lineage genes: *CD3D*, *CD4*, *CD8A*, and killer lectin-like receptors (figure 3C, online supplemental figure 5B,C).^{8 19 23 24} A final level of classification within lineages was defined by enriched expression of genes that commonly identify lymphocyte maturation and effector status (figure 3C-D). In total, we identified 14 subclasses; subclasses included cells from both radiated and control tumors (figure 3D-E, online supplemental table 5).

Four CD4⁺ T-cell lineage subclasses were defined by enrichment of gene expression regulators (figure 3D). Two of these clusters, CD4_FOS (high *FOS*, *JUNB* expression) and CD4_FOXP3 (high regulatory T cell (Treg) markers *FOXP3*, *IL2RA*) resembled previously defined T-cell subtypes in RCC.^{19 24} *FOXP3* expression was limited to the CD4_FOXP3 cluster (figure 3D) and represents the source of *FOXP3* in the broad immune analysis shown in online supplemental figure 4D. Further examination of CD4⁺ T cells (online supplemental figure 6A-C) showed enrichment of *FOXP3* among SBRT-treated cells. A comparison of the total lymphocyte composition between treatment groups showed a larger CD4_Treg proportion within the SBRT fraction compared with control (figure 3D,E) (χ^2 , $p < 2.2 \times 10^{-16}$). This is consistent with prior analysis of radiated RCC showing heightened levels of FOXP3⁺ cells.²²

CD8⁺ T-cell subclasses were delineated by the expression of activation and maturation markers (figure 3D). A naïve/stem-like subclass, CD8_TCF7, was defined by high *TCF7* (*TCF1*), *IL7R*, *CCR7*, and *SELL* (L-selectin) expression.²⁵ Exhaustion markers *PDCD1* (PD-1) and the terminal differentiation marker *TOX*, were increased among all other subclasses. An activated subclass, CD8_ITM2C, was categorized by high expression of *ITM2C*, which encodes a T-cell adhesion molecule, and *CD69*. This subclass transcriptionally resembles a 4-1BB-lo CD8⁺ T-cell subclass, which has been associated with ICB response.⁸ Additionally, the CD8_ITM2C subclass exhibited a PD-1-hi TIM3-lo LAG3-lo pattern of exhaustion

marker expression that is indicative of longer immune-related progression-free survival and objective response to ICB.²⁶ Three subclasses: CD8_CCR5, CD8_HAVCR2, and CD8_MKI67, showed pronounced expression of *IFNG*. CD8_HAVCR2 and CD8_MKI67, also had high co-expression of the T-cell effector *TNFSF10* (TRAIL) and the highest *TNFRSF9* (4-1BB) expression. Though past analysis of tumors associated TNFRSF9-hi CD8⁺ T cells with inferior overall survival,²⁷ high abundance of these cells is associated with improved progression-free survival in nivolumab-treated patients.²⁷ Similar to proliferating CD8⁺ T cells characterized through scRNAseq,^{19 28} the CD8_MKI67 subclass co-expressed cell proliferation markers, *MKI67* (KI67) and *TOP2A*, and showed the highest *TOX* expression. Previous analyses have associated high infiltration of proliferating CD8⁺ T cells with improved survival.²⁹

CD8⁺ T cells are increasingly activated in SBRT-treated RCC

We next performed a gross comparison of CD8⁺ T cells between treatment groups. Analysis by DGE showed increased levels of the naïve T-cell marker *IL7R* in control-RCC T cells (figure 4A). In contrast, effector molecules, *IFNG* and *TNFSF10*, maturation indicators, *CD69* and *PDCD1*; and the cell cycle marker *MKI67* were enriched among SBRT-RCC T cells (figure 4A), consistent with prior IHC analysis.²² The activation of SBRT-RCC CD8⁺ T cells was validated by the identification of T-cell receptor signaling, IFN- γ , and mitosis pathways through gene set enrichment analysis (GSEA) (figure 4B).

To analyze how radiation impacted maturation, we calculated pseudotime of our total CD8⁺ T-cell population (figure 4C,D).³⁰ The pseudotime was first validated by the polarized expression of naïve markers (*TCF7*, *CCR7*, *IL7R*) at the upper-left node, versus T-cell activation and exhaustion markers elsewhere in the plots (*ZFP36*, *PDCD1*, *TOX*) (figure 4C). This transcript analysis identified two lineages that both initiated at a naïve, CD8_TCF7 dense cluster and terminated at either CD8_CCR5 or CD8_MKI67 dominant cluster (figure 4D,E). The CD8_ITM2C subclass proceeded the CD8_TCF7-dominant starting node and just before the branchpoint between lineages (figure 4C). This pseudotemporal localization and high *CD69* early activation marker expression indicates that CD8_ITM2C cells may represent early-activated T cells derived from the stem-like population²⁵ and that, similar to stem-like T cells, its benefit may be as a precursor of effector T cells. We validated our distribution by tracking the expression of CD8⁺ T-cell maturation indicators across lineages (figure 4D,E). As in recent reports in RCC,¹⁹ the expression of stem-like and naïve T-cell genes *IL7R*, *TCF7*, and *CCR7* was highest near pseudotime=0 and decreased towards the lineage termini (figure 4E). The two lineages diverged with respect to expression of genes associated with the dominant subclass of the terminal node, *CCR5* or *MKI67*, respectively, (figure 4C-E).

We observed an unequal distribution of cells across pseudotime by treatment group (figure 4F). Control-RCC

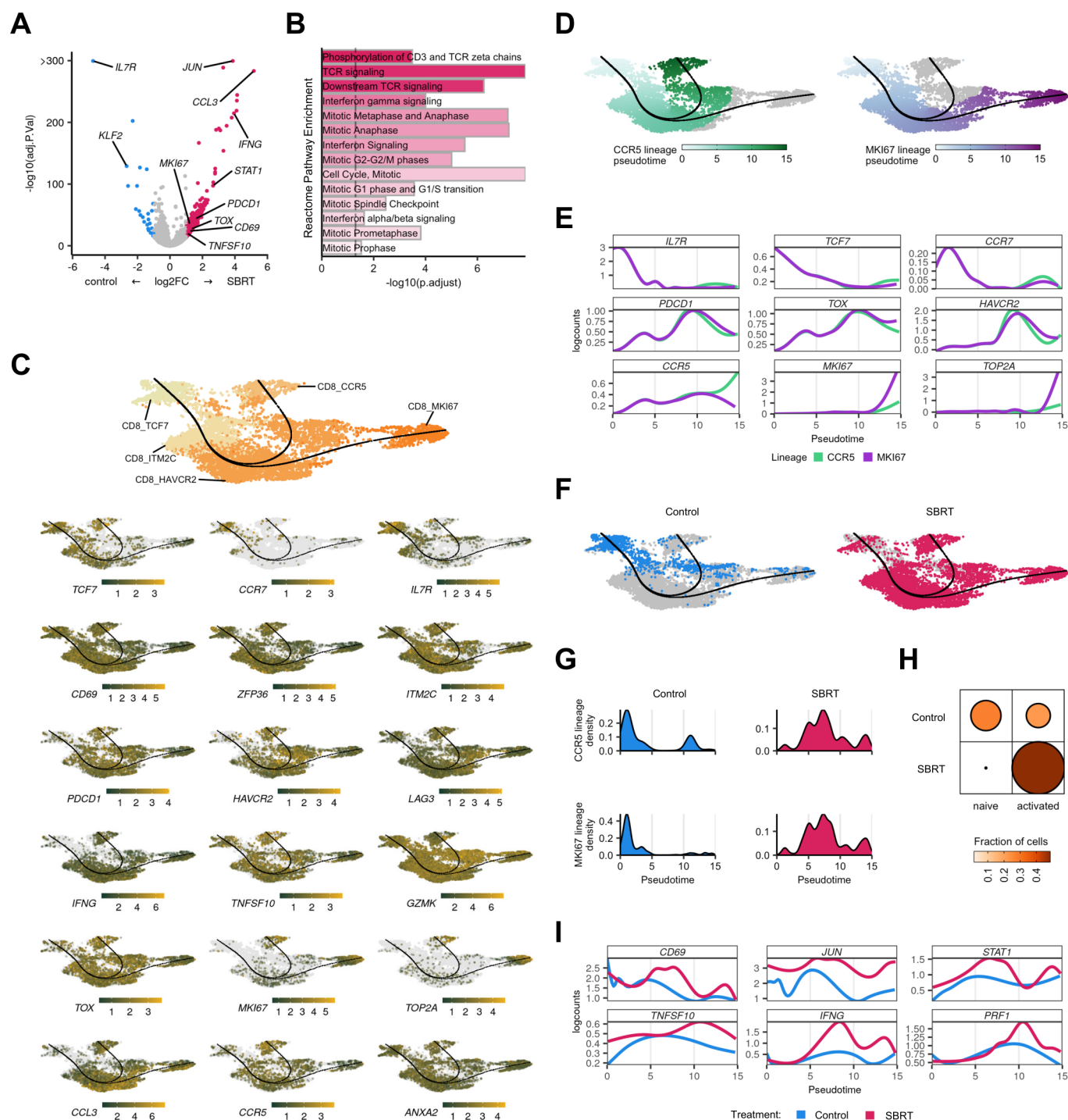


Figure 4 Increased CD8⁺ T-cell effector molecule expression following SBRT. (A) Volcano plot showing differential gene expression within CD8⁺ T cells between treatment groups. Color is differential gene expression, $|\log_2FC| > 1$; adjusted p value < 0.05 . (B) Gene set enrichment analysis of Reactome pathways. Opacity is NES. All shown pathways are significant, adjusted p value < 0.05 . (C) Pseudotime of CD8⁺ T cells showing distribution by CD8 subclass (top). Localized gene expression for indicated genes within the pseudotime plot (bottom). Gray has no detectable counts. (D) Pseudotime showing indicated CD8⁺ T-cell lineages. Color is calculated distribution for each lineage. (E) Pseudotemporal gene expression for each T-cell lineage. (F) Distribution of all captured cells by treatment group. (G) Distribution of cells by treatment group for each T-cell lineage. (H) Visualized χ^2 of naive and activated CD8⁺ T cells versus treatment group. Size and color show relative abundance after controlling for different total CD8⁺ T-cell numbers between treatment groups. (I) Pooled, pseudotemporal gene expression for each treatment group across lineages. SBRT, stereotactic body radiation therapy; NES, net enrichment score.

CD8⁺ T cells were concentrated near the CD8_TCF7 node at pseudotime=0, while SBRT-RCC CD8⁺ T cells were more widely dispersed, especially across transitional points and

at terminal nodes (figure 4G). Analysis across samples revealed consistent increased maturation in irradiated tumors (online supplemental figure 7). These findings

were strengthened by a comparison of T cells by subclass between treatment groups which showed the disproportionate distribution of control-RCC CD8⁺ T cells in the naïve T-cell subclass (figure 4H) (χ^2 , $p < 2.2 \times 10^{-16}$); a similar analysis of CD4⁺ T cells showed control-RCC CD4⁺ T cells were in the naïve, CD4_ANXA1 subclass (online supplemental figure 6C). Analysis of activation markers and associated transcription factors showed diverging expression patterns between treatment groups, with increasing expression of *CD69*, *JUN*, and *STAT1* at pseudotime=5 among SBRT-RCC CD8⁺ T cells (figure 4I); these preceded increases of *TNFSF10*, *IFNG*, and *PRF1* effector molecule expression in SBRT-RCC CD8⁺ T cells. Together, these data reveal that expression of critical effector molecules increased in CD8⁺ T-cell subclasses within the irradiated-RCC microenvironment.

SBRT-treated RCC has increased monocyte to macrophage polarization

Prior IHC analysis revealed increased levels of CD68⁺ macrophages in SBRT-treated tumors from this trial.²² Given the complexity of myeloid populations within RCC that can contain as many as 17 distinct macrophage phenotypes,³¹ we performed a more refined analysis to determine the impact of radiation on myeloid subsets (figure 5A). Myeloid cells were reclustered (online supplemental figure 8A) and then analyzed for hallmark gene expression (figure 5B,C, online supplemental figure 8B,C). Myeloid lineages were determined by high *S100A8* and *S100A9* expression for monocytes, high *APOE* and *APOC1* for macrophages, and high *CLEC10A* and *CLEC9A* for dendritic cells (DC), as in other published analyses^{8 19 23} (figure 5B,C). Lineage marker expression was largely uniform between treatment groups (online supplemental figure 8C). In total, we identified 16 myeloid subclasses; all but 1 included cells from both treatment groups. The relative abundance of monocytes, macrophages, and DCs were comparable to prior scRNAseq analyses in RCC.^{8 19} To examine if the myeloid subsets resembled myeloid-derived suppressor cell (MDSC) populations, we performed a transcriptional comparison against a publicly available gene signature.³² The MDSC signature was not enriched in the examined monocyte, macrophage, or DC subsets (online supplemental figure 9).

We noted that the classical and non-classical monocyte subclasses were either predominantly control-RCC or SBRT-RCC in origin (figure 5C,D). Among the macrophage subclasses, Mp_VEGFA was populated exclusively by SBRT-RCC cells (online supplemental figure 8C). DGE and GSEA of macrophages showed increased expression of hypoxia-associated genes and pathways in SBRT-RCC macrophages (online supplemental figure 10A-C), especially in the Mp_VEGFA subclass (online supplemental figure 10C). This hypoxia response may be driven in part by the limited number of detected blood vessels in SBRT-RCC versus control (online supplemental figure 4B). In addition to hypoxia, we identified the enrichment

of IFN signaling pathways (online supplemental figure 10B) in SBRT-RCC macrophages. Consistent with murine studies³³ an analysis of IFN response genes showed broad enrichment in macrophages from SBRT-treated tumors (online supplemental figure 10D), including *IRF8* enrichment which has been shown to predict survival of patients with RCC.³⁴

Having established CD8⁺ T cells as the main source of *IFNG* expression in the tumor microenvironment (online supplemental figure 4E), we employed a public database of predicted ligand-receptor and ligand-target gene interactors²⁰ to explore possible interactions between CD8⁺ T cells and RCC macrophages (online supplemental figure 10E). Referring to gene targets from established, macrophage-specific IFN-G response pathways (KEGG 05140, Dror *et al*),³⁵ we identified top predicted CD8⁺ T-cell ligands and potential macrophage receptors. IFN-G was the top CD8⁺ T-cell ligand for IFN-G response regulation in macrophages; although not among the top predicted ligands, we included IL-15 and IL-10 in this analysis as they have been previously used in CD8⁺ T cells to macrophage interaction analyses.¹⁹ Virtually all predicted CD8⁺ T-cell ligands as well as macrophage receptors and target genes were either significantly enriched or trended towards enrichment among the SBRT-RCC fraction (online supplemental figure 10E). Predicted ligands, *IFNG* in particular, had higher expression among CD8_HAVCR2 and CD8_MKI67 T cells (online supplemental figure 10E), suggesting that the MKI67 lineage may be a major contributor to IFN-G responses in macrophages. A reciprocal survey of T-cell co-regulatory molecule gene expression among macrophages was also performed. The costimulatory molecule CD86 and the T-cell inhibitory molecule galectin-9 (*LGALS9*) were both significantly enriched among macrophages within SBRT-treated RCC (online supplemental figure 10F).

Evaluation of myeloid polarization showed increased SBRT-RCC enrichment of MHC-II components and apolipoproteins (figure 6A). Further analysis revealed that SBRT-RCC myeloid cells enriched for both pro-inflammatory and anti-inflammatory marker genes (figure 6A,B). Regardless, it was evident that radiation resulted in overall macrophage polarization versus control (figure 6B).

For deeper analysis, we examined a pseudotime of all monocyte and macrophage cells subset from our data. Consistent with scRNAseq data in RCC,¹⁹ we identified two lineages that terminated at either non-classical monocyte or macrophage nodes (figure 6C). The classical and non-classical monocyte lineages had higher expression of *S100A9* while the macrophage lineage showed higher levels of MHC-II component expression, *APOE*, and *APOC1* (figure 6D). The macrophage lineage also expressed increased levels of *CD68* and *HLADRA* (figure 6E).

The distribution of cells by treatment group showed polarization across pseudotime. Specifically, control-RCC cells were more left-polarized, associated with monocytes,

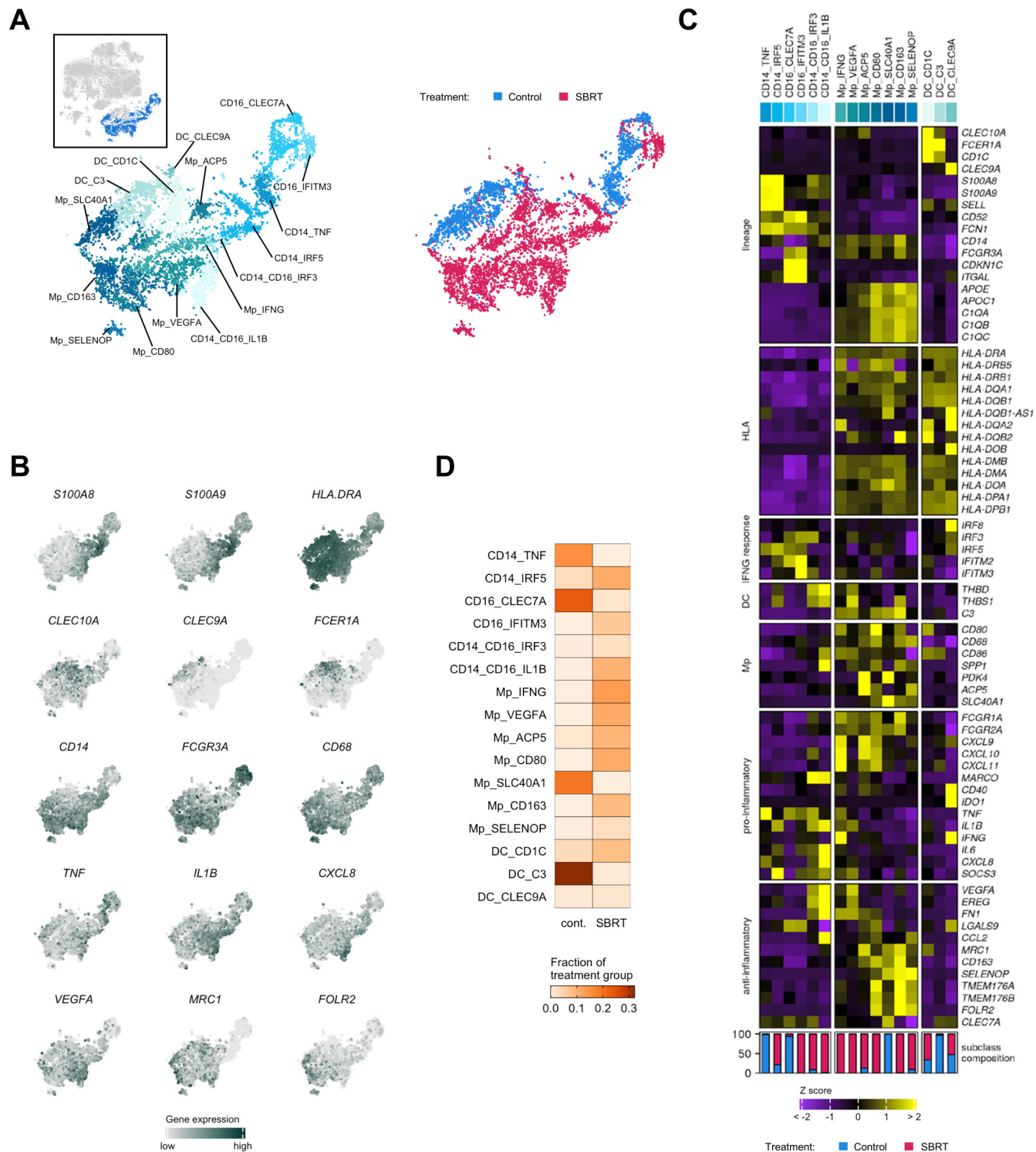


Figure 5 Analysis of myeloid cells by single-cell RNA sequencing. (A) Distribution of myeloid cells shown as subset from the t-SNE and by treatment group. Colors and labels correspond to cell subclassification (left) and treatment (right). Inset, showing cells subset from parent t-SNE for analysis. (B) Localized gene expression for indicated genes within the t-SNE. (C) Top, heatmap showing expression of genes used for myeloid subclassification. Bottom, bar graph showing subclass composition by treatment group after controlling for different total myeloid cell numbers between treatment groups. (D) Distribution of myeloid subclasses pooled within each treatment group. SBRT, stereotactic body radiation therapy; t-SNE, t-distributed stochastic neighbor embedding.

while SBRT-RCC cells were more polarized towards the macrophage terminal node (figure 6F). Analysis of myeloid subclass distribution showed a higher

macrophage to monocyte ratio in SBRT-RCC (figure 6G) (χ^2 , $p < 2.2 \times 10^{-16}$), which is consistent with IHC data

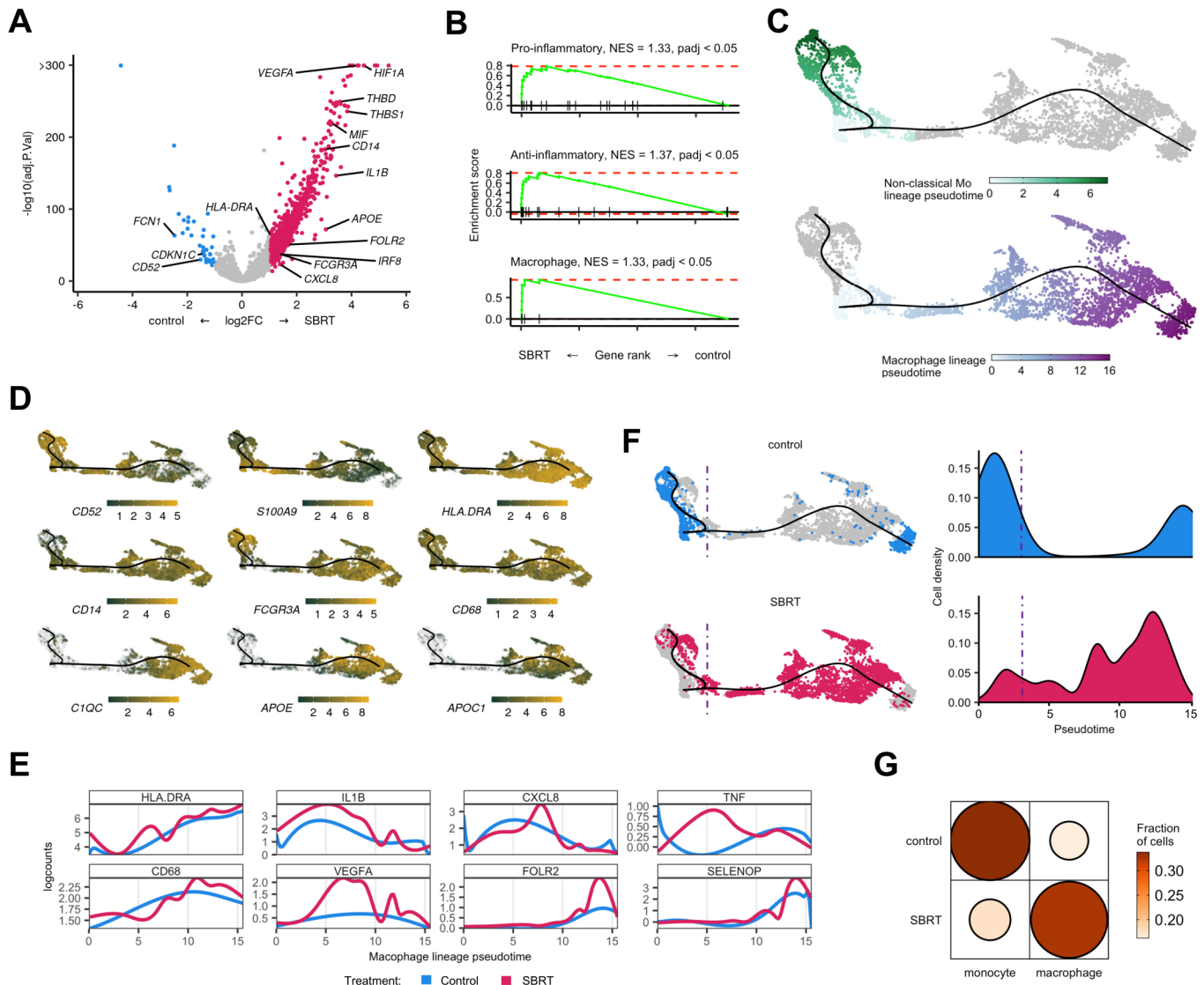


Figure 6 Transcript velocity analysis of myeloid populations shows increased differentiation toward macrophages in SBRT-treated tumors. (A) Volcano plot showing differential gene expression within monocytes and macrophages between treatment groups. Color is differential gene expression, $|\log_2FC| > 1$; adjusted p value < 0.05 . (B) Gene set enrichment analysis of curated pro-inflammatory, anti-inflammatory, and general macrophage gene lists. (C) Pseudotime showing indicated cell lineages. Color is calculated pseudotemporal distribution for each lineage. (D) Localized gene expression for indicated genes within the pseudotime plot. Gray has no detectable counts. (E) Pooled, pseudotemporal gene expression for each treatment group across the macrophage lineage. (F) Left, distribution of all captured cells by treatment group in the pseudotime. Right, distribution cells by treatment group for the macrophage lineage. (G) Visualized chi square of monocytes and macrophages versus treatment group. Size and color show relative abundance after controlling for different summed monocytes and macrophages between treatment groups. SBRT, stereotactic body radiation therapy; NES, net enrichment score.

demonstrating increased macrophage abundance in irradiated tumors from this trial.²²

Increased effector CD8⁺ T-cell interaction potential in SBRT-RCC

To determine the effect of radiation on tumor cells treated in situ, we calculated DGE and GSEA for the tumor subset (figure 7A–D). SBRT-RCC tumor cells had increased expression of tumor associated antigen genes, *MUC1* and *CA9*, as well as *CALR*. MHC components *HLA-A*, *HLA-B*, *HLA-E*, and *HLA-G* were also higher in SBRT-RCC by DGE analysis (figure 7C). Further, antigen presentation pathways were enriched among irradiated tumor

cells (figure 7D). While previous reports of bulk RNA sequencing analysis¹³ did not show significant changes post-SBRT for the aforementioned genes (*MUC1*, *CA9* and *CALR*), these scRNAseq findings are consistent with flow cytometric analysis of irradiated RCC tumors¹³ and highlight the advantage of compartment-specific analysis. We also observed increased expression of apoptotic regulators *BAD* and *BAX* (figure 7C) and apoptosis pathway enrichment within irradiated RCC (figure 7D).

SBRT-RCC cells showed higher expression of the IFN- γ receptor component *IFNGR1*, as well as IFN- γ response genes including: *IFI27*, *IFI16*, *IFI6* (figure 7C) and

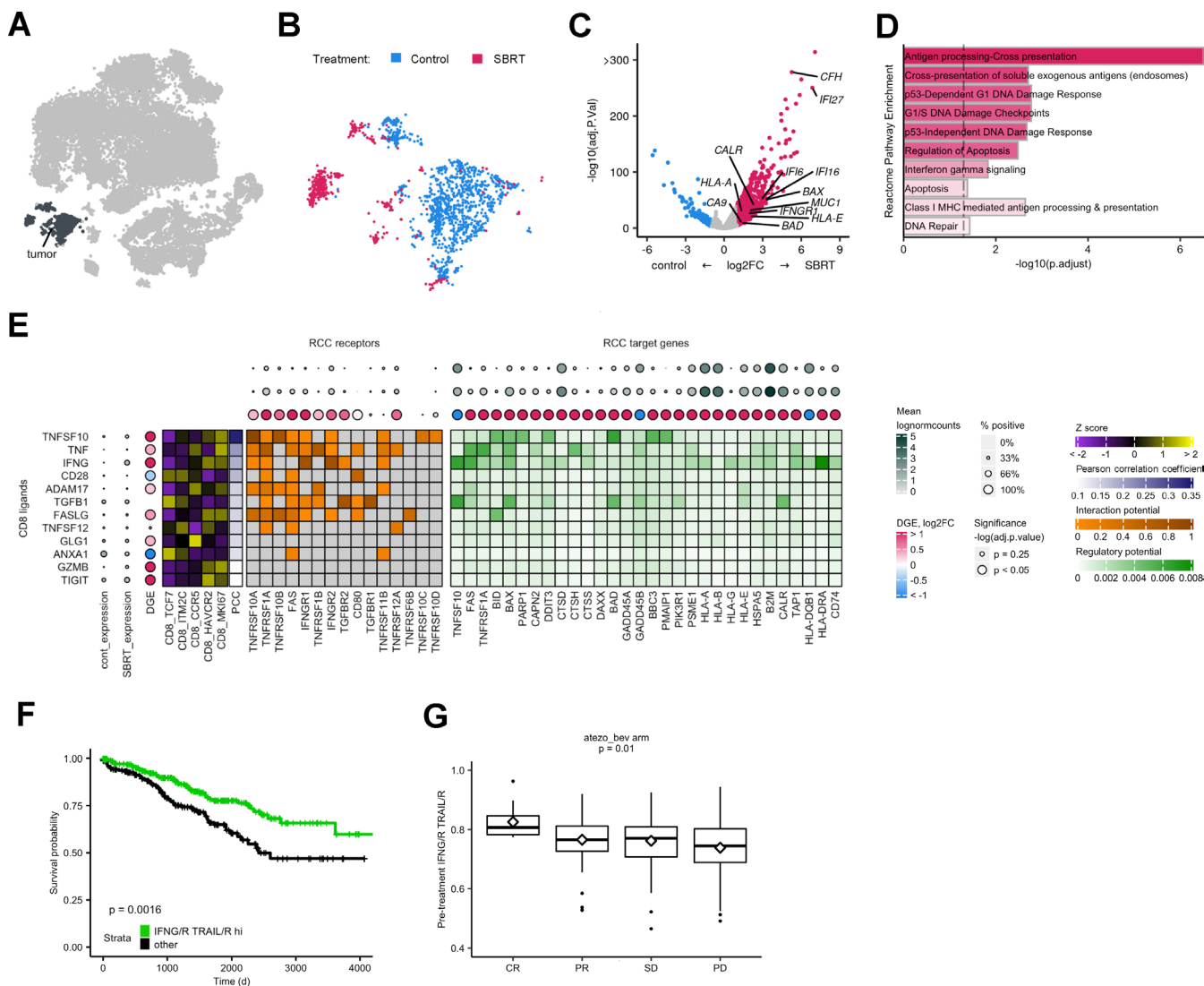


Figure 7 Analysis of SBRT cancer cells shows enriched antigen presentation and increased interactions with CD8⁺ T cells. (A) Tumor cells subset from parent t-SNE for analysis. (B) Distribution of cells by treatment group. (C) Volcano plot showing DGE within CD8⁺ T cells between treatment groups. Color is differential gene expression, $|\text{abs}(\log_2\text{FC})| > 1$; adjusted p value < 0.05 . (D) Gene set enrichment analysis of Reactome pathways. Opacity is NES. All shown pathways are significant, adjusted p value < 0.05 . (E) Predicted interactions from CD8 ligands to tumor cell receptors and target genes. CD8 ligands are ordered by decreasing correlation to target gene expression, PCC. Z score shows expression of CD8 ligands by subclass. DGE is calculated separately for either the CD8 or tumor subsets. (F) Kaplan-Meier curve showing survival with respect to IFN-G/R TRAIL/R hi patient classification. HR of IFN-G/R-hi-and-TRAIL/R-hi=0.55. (G) Box plots showing IFN-G/R, TRAIL/R score in pre-immune checkpoint blockade treatment patient tumors. Middle represents the median; hinges describe the first quartile and third quartile; whiskers show $\pm 1.5 \times \text{IQR}$; diamond is the mean. P value calculated by analysis of variance. t-SNE, t-distributed stochastic neighbor embedding; DEG, differential gene expression; IFN, interferon; RCC, renal cell carcinoma; SBRT, stereotactic body radiation therapy; NES, net enrichment score; CR, complete response; PR, partial response; SD, stable disease; PD, progressive disease; PCC, pearson correlation coefficient.

pathway enrichment of IFN-G signaling (figure 7D). To further characterize the IFN-G response in tumor cells, we examined previously described, antagonistic hallmark IFN-G response and IFN-G resistance pathways³⁶ (online supplemental figure 11A,B) and found both were enriched among radiated fractions. We next examined whether hallmark IFN-G and resistance pathways are expressed in distinct tumor cell populations and found both signals to be highly correlated (Pearson correlation

coefficient=0.73; $p < 2.2 \times 10^{-16}$) (online supplemental figure 11C).

Given the increased indicators of T cell-mediated cell death among radiated tumor cells, including antigen presentation and apoptosis pathways, we examined how CD8⁺ T cells might be driving this response. Using genes from well characterized pathways for antigen processing and presentation (KEGG 04612) as well as apoptosis (KEGG 04210), we identified TRAIL (*TNFSF10*) and

IFN- γ among the top predicted CD8⁺ T-cell ligands for these tumor cell responses (figure 7E). Expression of the CD8⁺ T-cell ligands, *IFNG* and *TRAIL*, as well as their receptor components *IFNGR1* and *TNFRSF10A* were significantly enriched or trended towards enrichment with SBRT-treatment; additionally, almost all differentially expressed tumor target genes were SBRT-enriched (figure 7E). Ligands for tumor antigen presentation and apoptosis, IFN- γ and TRAIL, showed higher expression among CD8_HAVCR2 and CD8_MKI67 CD8⁺ T cells (figure 7E). This was similar to an analysis of CD8⁺ T-cell drivers of IFN- γ responses in macrophages (online supplemental figure 10E).

To determine clinical relevance of these putative immunogenic interactions between CD8⁺ T cells and cancer cells, we analyzed TCGA data. Selected patients with RCC were classified based on expression of IFN- γ and TRAIL ligands and receptors (online supplemental figure 12A); roughly half of patients were classified as IFN- γ /R and TRAIL/R hi. Our analysis showed IFN- γ , TRAIL hi patients had improved overall survival (figure 7F, online supplemental figure 12B). Because of significant interest in radiation as a tumor-priming treatment for paired immunotherapy, we next examined pre-ICB treatment bulk RNA with matched clinical response data.³⁷ We found that IFN- γ , TRAIL ligand and receptor expression correlated with clinical response after ICB (figure 7G).

DISCUSSION

To improve radiation-induced immunogenicity and optimize treatment regimens, investigators continue to probe how radiation impacts antigenicity and neoantigen expression,^{38 39} immune infiltration,¹⁶ and induction of IFN pathways.¹⁷ Clinical observations have shown that patients treated with ICB may benefit from preconditioning radiation even months prior to the administration of immunotherapy,⁴⁰ suggesting that radiation has long-lasting immune effects. Sequencing of radiation with immune-based treatments has been demonstrated to be critical for responses in preclinical models.⁴¹

Central to each of these investigations and potential synergy with ICB is the status of CD8⁺ T cells following radiotherapy. Intratumoral CD8⁺ T cells are a heterogeneous population consisting of subsets with distinct functions, transcriptional states, and proliferative capacity.²⁵ Through the data presented here we address questions regarding the cell type-specific effects of radiation in patient tumors and build on the transcriptomic atlas of human tumors.^{8 19 24 28} Analysis of radiotherapy-treated tumors showed a redistribution from naïve-like lymphocytes to more mature states. Comparison of CD8⁺ T cells between treatment groups showed broad enrichment of effector and activation marker expression with radiation, including IFN- γ .

A critical, unanswered question relates to the mechanism(s) driving increased proportions of effector T cells in SBRT-treated tumors. Differential radioresistance of

immune subsets could play a role in our observations. For example, naïve or stem-like CD8⁺ T cells were shown to be more sensitive to radiation than memory, effector, or recently activated T cells.^{42 43} Radiosensitivity can also be impacted by the microenvironment, with tumor-resident populations receiving relative protection compared with CD8⁺ T cells found in circulation or lymph nodes.⁴⁴ In this instance, intratumoral T cells treated with a similar high dose of radiation were found to produce more IFN- γ on a per cell basis reflecting the results of our pseudotime analysis. Our previous evaluation of peripheral blood samples demonstrated heightened levels of tumor-enriched clones 2 weeks after radiation.¹³ Recent work evaluating radiotherapy of patient lung metastases has shown elevated levels of PD-1⁺ T-cell subsets in the periphery following single-fraction treatment.⁴⁵ Collectively, these findings suggest that T-cell activation occurring outside of the irradiated field could also be a driver of changes later observed in the tumor microenvironment.

Analysis of tumor cells showed increased antigen and MHC-I component expression in radiated samples, supporting enhanced immunogenicity in irradiated tumors. The data also permitted an examination of potential cell-to-cell interactions within the tumor microenvironment, suggesting that specific CD8⁺ T subsets were drivers of increased antigen presentation in tumor cells. We identified receptor and ligand interactions, largely enriched within radiated tumors, between IFN- γ /R and TRAIL/R. Expression levels of these ligand and receptor pairs were associated with overall survival and response to ICB. These findings are noteworthy considering recent studies showing increased immune activity following radiation is reliant on upregulation of MHC molecules as well as TRAIL-mediated interactions.⁴⁶ Implications may extend to other cancer therapies including chemotherapeutic agents which have long shown the capacity to increase expression of TRAIL receptors DR4 and DR5.⁴⁷ Our findings also show enrichment of *FOXP3* Treg within radiated RCC. Given prior work has revealed spatial and proportional correlation between activated CD8 T cells and Treg in human tumors,⁴⁸ this immunosuppressive population could be a therapeutic target in combination radiation regimens.

While this study provides much needed resolution to previous, bulk RNA data from radiated RCC,¹³ certain limitations remain. Chromatin regulators are commonly mutated in RCC impacting expression of large numbers of genes.⁴⁹ Future studies are therefore warranted to interrogate the relationship between radiation-induced immunologic changes and tumor mutational status. Statistical analyses of unpaired samples may have missed more subtle, but nevertheless important, changes on-treatment that could have been found with more powerful tests afforded by additional samples. Cancer cells are sensitive to reagents and the process used to obtain single-cell preparations from RCC,¹⁹ and thus are under-represented in our analysis. More broadly, samples for this study were collected 4 weeks after 15 Gy radiation in a single arm

trial, and thus leave important questions regarding the acute effects and kinetics of immune activity as well as dose fractionation unanswered.⁵⁰ Our findings in RCC, which represents a highly immune infiltrated and vascularized malignancy,²¹ may not extend to other tumor types. Finally, this report provides a glimpse of the irradiated tumor immune landscape. However, since patients received varying adjuvant treatments after their time on the trial it is not feasible to correlate outcomes with changes in the tumor after SBRT.

Collectively these findings denote the contributions of immune and tumor-intrinsic contributions towards radiation-induced tumor immunogenicity. Our data showing increased levels of effector and proliferating CD8⁺ T cells in SBRT-treated RCC support prior studies that demonstrated heightened T-cell clonality within this tumor microenvironment.¹³ Further evaluation of radiation-induced changes to patient tumors and systemic immune responses are required to provide rationale for optimal design of clinical strategies that will precondition with radiation and then treat with ICB or other immunotherapy combinations.

Acknowledgements We sincerely thank all the patients and their families involved in this study. Research reported here was supported by the Roswell Park Friends of Urology and the Elsa Kreiner Memorial Fund. We would also like to thank Hans Minderman, Orla Maguire, and Joseph Hanson for their assistance in development of the spectral flow cytometry panel and corresponding acquisition and analysis.

Contributors JC, AK, AKS, and JBM designed the study. JC, AK, MG, BJW, KTS, AC, PKW, and JBM developed methodology. Research was performed by JC, AK, MG, BJW, AKS, and JBM. Data was analyzed by JC, AK, MG, BJW, and JBM. JC, AK, and JBM wrote the manuscript with input from all coauthors. JC, AK, MG, BJW, TS, EAR, SIA, AKS, and JBM edited the manuscript. JBM is guarantor for this work.

Funding Research reported in this publication was supported by a DOD Kidney Cancer Research Program Idea Development Award (W81XWH2010720). This project was also supported by the National Center for Advancing Translational Sciences of the National Institutes of Health under award number UL1TR001412 to the University at Buffalo. The content is solely the responsibility of the authors and does not necessarily represent the official views of the NIH. Support was also provided by the National Cancer Institute (Grant P30CA016056 supporting use of the Roswell Park Comprehensive Cancer Center's Bioinformatics, Genomics, Pathology Network, Atlas Studios as well as Flow and Image Cytometry Shared Resources).

Competing interests None declared.

Patient consent for publication Not applicable.

Ethics approval This study involves human participants and was approved by the Roswell Park Institutional Review Board for the clinical trial under number I 212712. The evaluation of de-identified patient samples from that trial shown in this manuscript was approved under BDR 053514 as non-human subject research also by the Roswell Park Institutional Review Board. The research activity was reviewed and determined to be non-human subject research (NHSR). The department of health and human services does not consider research involving data and specimens to involve human subjects as defined under 45 CFR 46.102 (f) if the following conditions are met: (1) The private information or specimens were not collected specifically for the currently proposed research project through an interaction or intervention with living individuals; and (2) The investigator(s) cannot readily ascertain the identity of the individual(s) to whom the coded private information or specimens pertain. The Office of Research Subject Protection at Roswell Park therefore stated that in accordance with 45 CFR 46.102 of the Common Rule, the protocol used to analyze samples in this study does not involve human subject research. Participants gave informed consent to participate in the study before taking part.

Provenance and peer review Not commissioned; externally peer reviewed.

Data availability statement Data are available in a public, open access repository. All data relevant to the study are included in the article or uploaded as supplementary information. Single-cell RNA-sequencing data sets generated are available on GEO database (GSE202374). Patient response data were from the European Genome-Phenome Archive (EGA) under accession number EGAS00001002928. Annotated single-cell RNA data sets and TCGA barcodes of all KIRC samples are deposited in GitHub (github.com/JackylChow/Chow_et_al_JITC_2023). Spectral flow cytometry data are available in ImmPort under access code SDY1998.

Supplemental material This content has been supplied by the author(s). It has not been vetted by BMJ Publishing Group Limited (BMJ) and may not have been peer-reviewed. Any opinions or recommendations discussed are solely those of the author(s) and are not endorsed by BMJ. BMJ disclaims all liability and responsibility arising from any reliance placed on the content. Where the content includes any translated material, BMJ does not warrant the accuracy and reliability of the translations (including but not limited to local regulations, clinical guidelines, terminology, drug names and drug dosages), and is not responsible for any error and/or omissions arising from translation and adaptation or otherwise.

Open access This is an open access article distributed in accordance with the Creative Commons Attribution Non Commercial (CC BY-NC 4.0) license, which permits others to distribute, remix, adapt, build upon this work non-commercially, and license their derivative works on different terms, provided the original work is properly cited, appropriate credit is given, any changes made indicated, and the use is non-commercial. See <http://creativecommons.org/licenses/by-nc/4.0/>.

ORCID iDs

Jacky Chow <http://orcid.org/0000-0002-3849-0346>

Adil Khan <http://orcid.org/0000-0002-0717-3268>

Scott I Abrams <http://orcid.org/0000-0002-8742-4708>

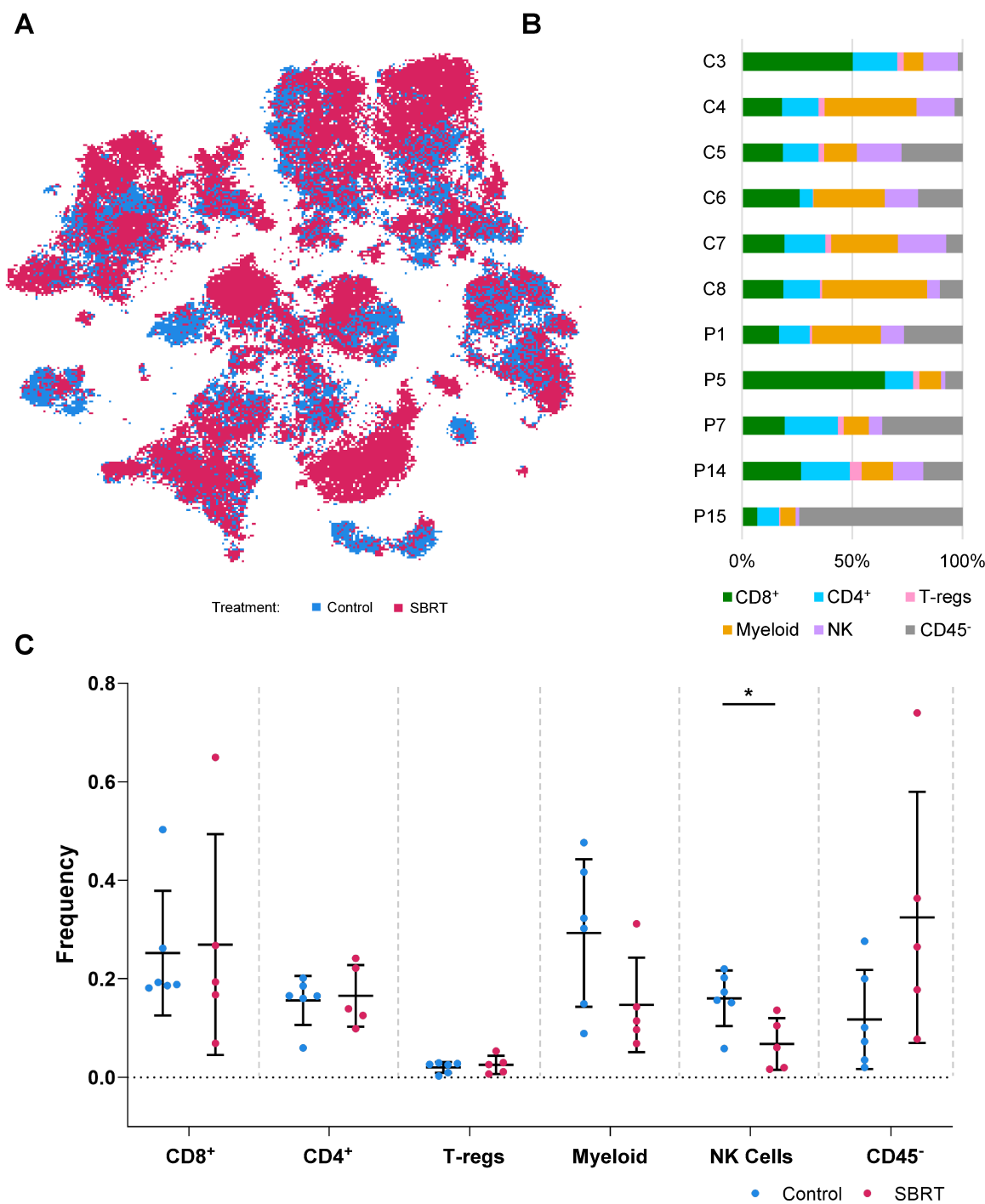
Anurag K Singh <http://orcid.org/0000-0002-6703-5115>

Jason B Muhitch <http://orcid.org/0000-0002-7703-1425>

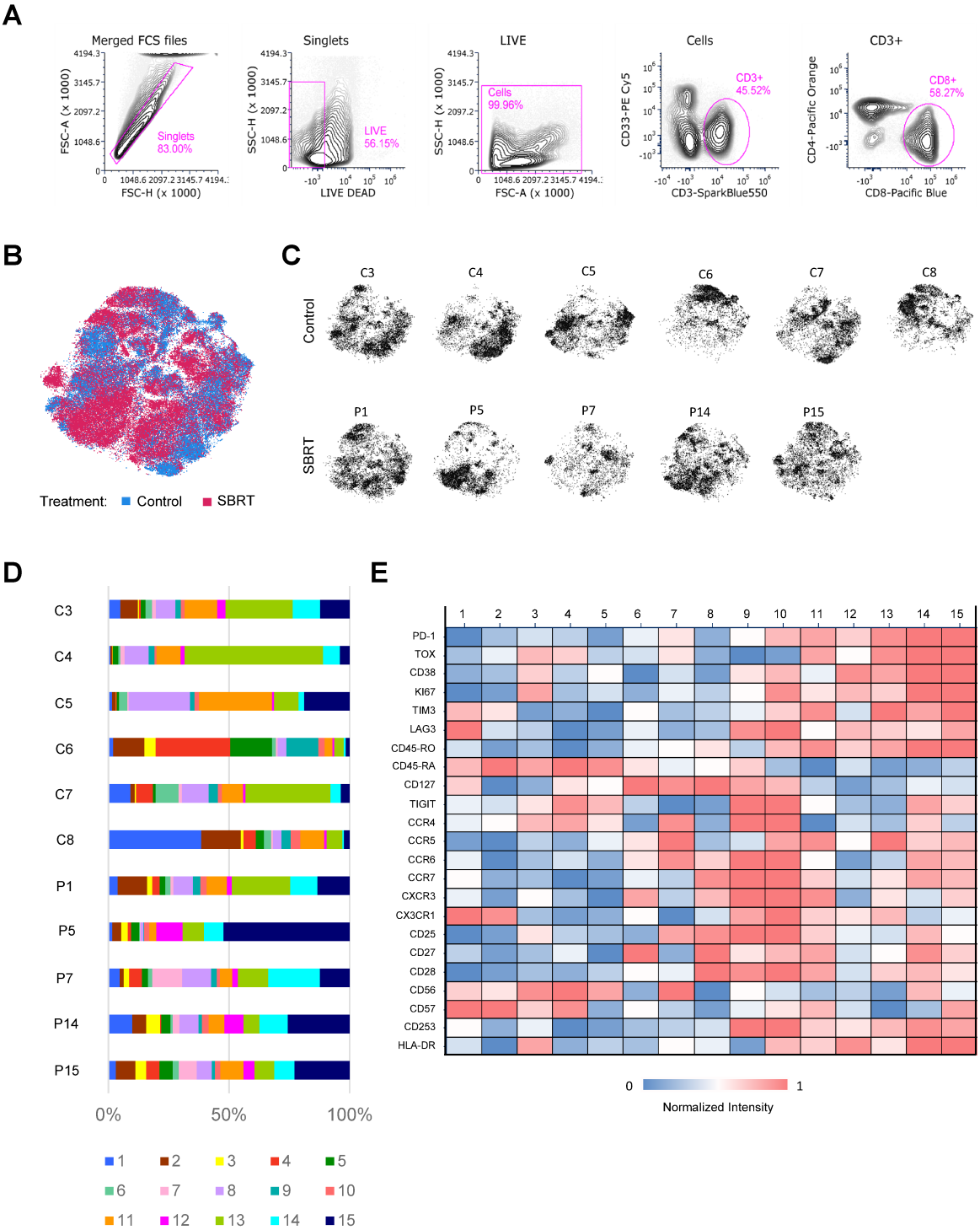
REFERENCES

- Seung SK, Curti BD, Crittenden M, et al. Phase 1 study of stereotactic body radiotherapy and interleukin-2 -- tumor and immunological responses. *Sci Transl Med* 2012;4:137ra74.
- Formenti SC, Rudqvist N-P, Golden E, et al. Radiotherapy induces responses of lung cancer to CTLA-4 blockade. *Nat Med* 2018;24:1845–51.
- Siva S, Bressel M, Wood ST, et al. Stereotactic radiotherapy and short-course pembrolizumab for oligometastatic renal cell carcinoma—the RAPPORT trial. *European Urology* 2022;81:364–72.
- Theelen WSME, Peulen HMU, Lalezari F, et al. Effect of pembrolizumab after stereotactic body radiotherapy vs pembrolizumab alone on tumor response in patients with advanced non-small cell lung cancer: results of the PEMBRO-RT phase 2 randomized clinical trial. *JAMA Oncol* 2019;5:1276–82.
- Ali M, Mooi J, Lawrentschuk N, et al. The role of stereotactic ablative body radiotherapy in renal cell carcinoma. *European Urology* 2022;82:613–22.
- Jagodinsky JC, Harari PM, Morris ZS. The promise of combining radiation therapy with immunotherapy. *Int J Radiat Oncol Biol Phys* 2020;108:6–16.
- De Martino M, Daviaud C, Vanpouille-Box C. Radiotherapy: an immune response modifier for immuno-oncology. *Semin Immunol* 2021;52:101474.
- Bi K, He MX, Bakouny Z, et al. Tumor and immune reprogramming during immunotherapy in advanced renal cell carcinoma. *Cancer Cell* 2021;39:649–61.
- van der Woude LL, Gorris MAJ, Wortel IMN, et al. Tumor microenvironment shows an immunological abscopal effect in patients with NSCLC treated with pembrolizumab-radiotherapy combination. *J Immunother Cancer* 2022;10:e005248.
- Ayers M, Lunceford J, Nebozhyn M, et al. IFN-γ-related mRNA profile predicts clinical response to pd-1 blockade. *J Clin Invest* 2017;127:2930–40.
- Luke JJ, Lemons JM, Karrison TG, et al. Safety and clinical activity of pembrolizumab and multisite stereotactic body radiotherapy in patients with advanced solid tumors. *JCO* 2018;36:1611–8.
- Herrera FG, Ronet C, Ochoa de Olza M, et al. Low-dose radiotherapy reverses tumor immune desertification and resistance to immunotherapy. *Cancer Discov* 2022;12:108–33.
- Chow J, Hoffend NC, Abrams SI, et al. Radiation induces dynamic changes to the T cell repertoire in renal cell carcinoma patients. *Proc Natl Acad Sci U S A* 2020;117:23721–9.

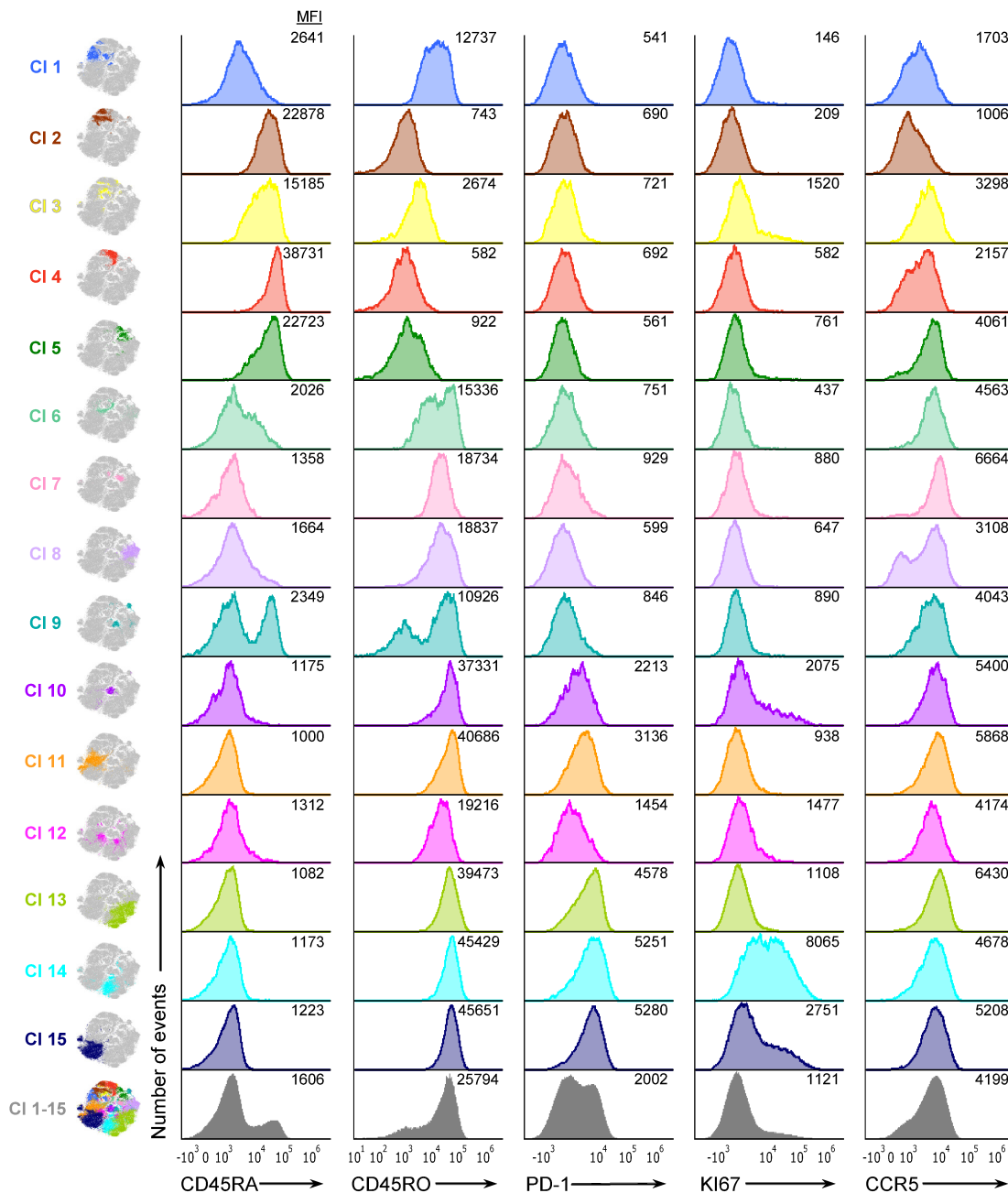
- 14 Mills BN, Qiu H, Drage MG, *et al.* Modulation of the human pancreatic ductal adenocarcinoma immune microenvironment by stereotactic body radiotherapy. *Clin Cancer Res* 2022;28:150–62.
- 15 Farren MR, Sayegh L, Ware MB, *et al.* Immunologic alterations in the pancreatic cancer microenvironment of patients treated with neoadjuvant chemotherapy and radiotherapy. *JCI Insight* 2020;5:e130362.
- 16 Lim JYH, Gerber SA, Murphy SP, *et al.* Type I interferons induced by radiation therapy mediate recruitment and effector function of CD8 (+) T cells. *Cancer Immunol Immunother* 2014;63:259–71.
- 17 Vanpouille-Box C, Alard A, Aryankalayil MJ, *et al.* Dna exonuclease TREX1 regulates radiotherapy-induced tumour immunogenicity. *Nat Commun* 2017;8:15618.
- 18 Street K, Risso D, Fletcher RB, *et al.* Slingshot: cell lineage and pseudotime inference for single-cell transcriptomics. *BMC Genomics* 2018;19:477.
- 19 Braun DA, Street K, Burke KP, *et al.* Progressive immune dysfunction with advancing disease stage in renal cell carcinoma. *Cancer Cell* 2021;39:632–48.
- 20 Browaeys R, Saelens W, Saeys Y. NicheNet: modeling intercellular communication by linking ligands to target genes. *Nat Methods* 2020;17:159–62.
- 21 Motzer RJ, Banchereau R, Hamidi H, *et al.* Molecular subsets in renal cancer determine outcome to checkpoint and angiogenesis blockade. *Cancer Cell* 2020;38:803–17.
- 22 Singh AK, Winslow TB, Kermany MH, *et al.* A pilot study of stereotactic body radiation therapy combined with cytoreductive nephrectomy for metastatic renal cell carcinoma. *Clin Cancer Res* 2017;23:5055–65.
- 23 Borchering N, Vishwakarma A, Voigt AP, *et al.* Mapping the immune environment in clear cell renal carcinoma by single-cell genomics. *Commun Biol* 2021;4:122.
- 24 Zhang L, Li Z, Skrzypczynska KM, *et al.* Single-cell analyses inform mechanisms of myeloid-targeted therapies in colon cancer. *Cell* 2020;181:442–59.
- 25 Jansen CS, Prokhnevskaya N, Master VA, *et al.* An intra-tumoral niche maintains and differentiates stem-like CD8 T cells. *Nature* 2019;576:465–70.
- 26 Pignon J-C, Jegede O, Shukla SA, *et al.* IrRECIST for the evaluation of candidate biomarkers of response to nivolumab in metastatic clear cell renal cell carcinoma: analysis of a phase II prospective clinical trial. *Clin Cancer Res* 2019;25:2174–84.
- 27 Li Y, Wang Z, Jiang W, *et al.* Tumor-infiltrating TNFRSF9⁺ CD8⁺ T cells define different subsets of clear cell renal cell carcinoma with prognosis and immunotherapeutic response. *Oncimmunology* 2020;9:1838141.
- 28 Krishna C, DiNatale RG, Kuo F, *et al.* Single-cell sequencing links multiregional immune landscapes and tissue-resident t cells in ccrcc to tumor topology and therapy efficacy. *Cancer Cell* 2021;39:662–77.
- 29 Nakano O, Sato M, Naito Y, *et al.* Proliferative activity of intratumoral CD8 (+) T-lymphocytes as a prognostic factor in human renal cell carcinoma: clinicopathologic demonstration of antitumor immunity. *Cancer Res* 2001;61:5132–6.
- 30 La Manno G, Soldatov R, Zeisel A, *et al.* Rna velocity of single cells. *Nature* 2018;560:494–8.
- 31 Chevrier S, Levine JH, Zanotelli VRT, *et al.* An immune atlas of clear cell renal cell carcinoma. *Cell* 2017;169:736–49.
- 32 Alshetaiwi H, Pervolarakis N, McIntyre LL, *et al.* Defining the emergence of myeloid-derived suppressor cells in breast cancer using single-cell transcriptomics. *Sci Immunol* 2020;5:eaay6017.
- 33 Wisdom AJ, Mowery YM, Hong CS, *et al.* Single cell analysis reveals distinct immune landscapes in transplant and primary sarcomas that determine response or resistance to immunotherapy. *Nat Commun* 2020;11:6410.
- 34 Muhitch JB, Hoffend NC, Azabdaftari G, *et al.* Tumor-associated macrophage expression of interferon regulatory factor-8 (irf8) is a predictor of progression and patient survival in renal cell carcinoma. *J Immunother Cancer* 2019;7:155.
- 35 Dror N, Alter-Koltunoff M, Azriel A, *et al.* Identification of IRF-8 and IRF-1 target genes in activated macrophages. *Mol Immunol* 2007;44:338–46.
- 36 Benci JL, Johnson LR, Choa R, *et al.* Opposing functions of interferon coordinate adaptive and innate immune responses to cancer immune checkpoint blockade. *Cell* 2019;178:933–48.
- 37 Rini BI, Powles T, Atkins MB, *et al.* Atezolizumab plus bevacizumab versus sunitinib in patients with previously untreated metastatic renal cell carcinoma (immotion151): a multicentre, open-label, phase 3, randomised controlled trial. *Lancet* 2019;393:2404–15.
- 38 Reits EA, Hodge JW, Herberts CA, *et al.* Radiation modulates the peptide repertoire, enhances MHC class I expression, and induces successful antitumor immunotherapy. *J Exp Med* 2006;203:1259–71.
- 39 Lussier DM, Alspach E, Ward JP, *et al.* Radiation-induced neoantigens broaden the immunotherapeutic window of cancers with low mutational loads. *Proc Natl Acad Sci U S A* 2021;118:e2102611118.
- 40 Shaverdian N, Lisberg AE, Bornazyan K, *et al.* Previous radiotherapy and the clinical activity and toxicity of pembrolizumab in the treatment of non-small-cell lung cancer: a secondary analysis of the KEYNOTE-001 phase 1 trial. *Lancet Oncol* 2017;18:895–903.
- 41 Wei J, Montalvo-Ortiz W, Yu L, *et al.* Sequence of α pd-1 relative to local tumor irradiation determines the induction of abscopal antitumor immune responses. *Sci Immunol* 2021;6:eabg0117.
- 42 Grayson JM, Harrington LE, Lanier JG, *et al.* Differential sensitivity of naive and memory CD8⁺ T cells to apoptosis in vivo. *The Journal of Immunology* 2002;169:3760–70.
- 43 Dunn PL, North RJ. Adoptive immunotherapy of established tumors. acquisition of radioresistance by tumor-specific T cells after passive transfer into tumor-bearing recipients. *Int J Cancer* 1994;57:592–7.
- 44 Arina A, Beckett M, Fernandez C, *et al.* Tumor-reprogrammed resident T cells resist radiation to control tumors. *Nat Commun* 2019;10:3959.
- 45 Siva S, Bressel M, Mai T, *et al.* Single-fraction vs multifraction stereotactic ablative body radiotherapy for pulmonary oligometastases (SAFRON II): the trans tasman radiation oncology group 13.01 phase 2 randomized clinical trial. *JAMA Oncol* 2021;7:1476–85.
- 46 Lhuillier C, Rudqvist N-P, Yamazaki T, *et al.* Radiotherapy-exposed CD8⁺ and CD4⁺ neoantigens enhance tumor control. *J Clin Invest* 2021;131:e138740.
- 47 Gibson SB, Oyer R, Spalding AC, *et al.* Increased expression of death receptors 4 and 5 synergizes the apoptosis response to combined treatment with etoposide and TRAIL. *Mol Cell Biol* 2000;20:205–12.
- 48 Ji AL, Rubin AJ, Thrane K, *et al.* Multimodal analysis of composition and spatial architecture in human squamous cell carcinoma. *Cell* 2020;182:497–514.
- 49 Cancer Genome Atlas Research N. Comprehensive molecular characterization of clear cell renal cell carcinoma. *Nature* 2013;499:43–9.
- 50 Demaria S, Guha C, Schoenfeld J, *et al.* Radiation dose and fraction in immunotherapy: one-size regimen does not fit all settings, so how does one choose? *J Immunother Cancer* 2021;9:e002038.



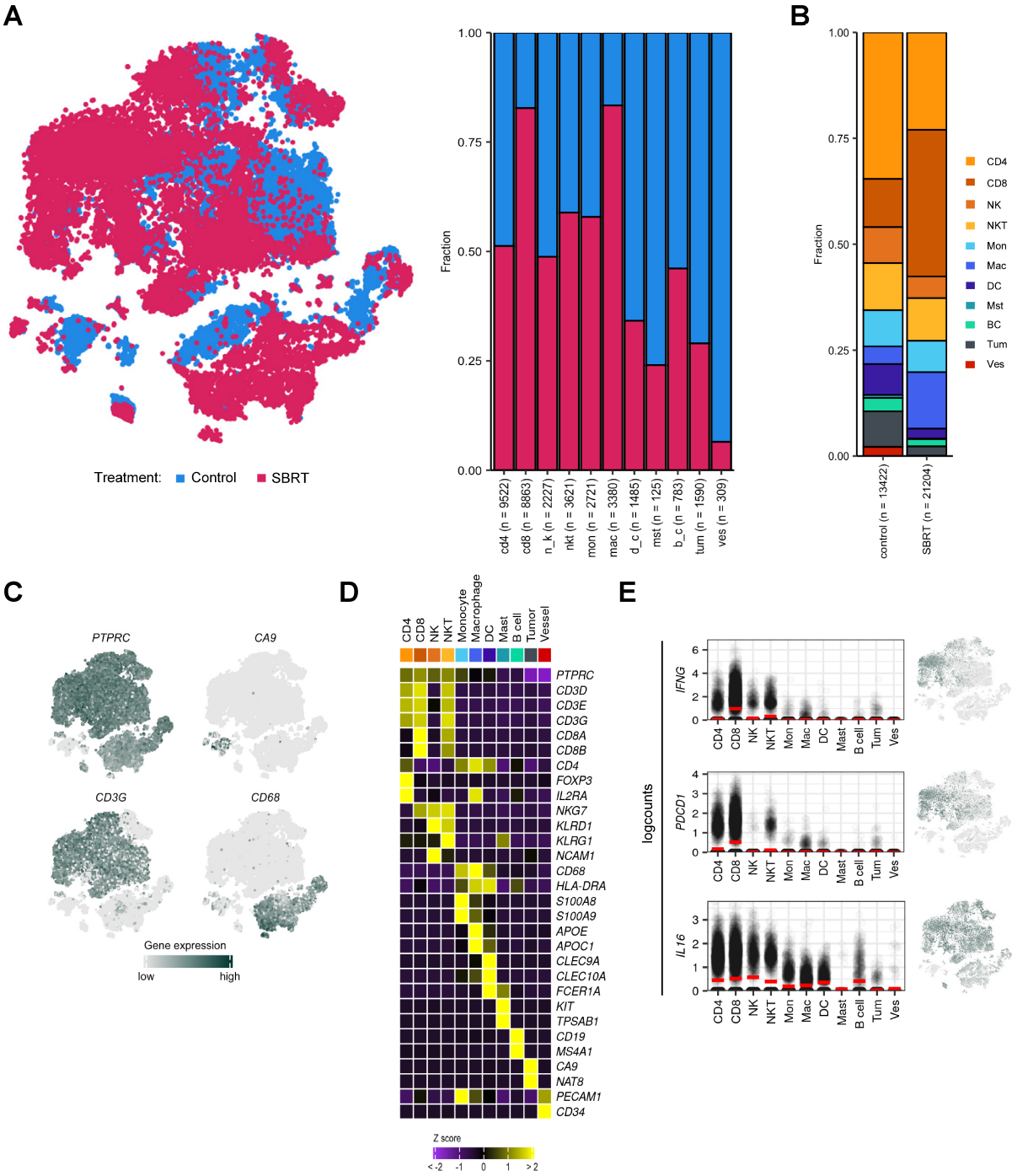
Supplemental Figure 1. Comparison of control vs SBRT treated cells by spectral flow cytometry. (A) t-SNE overlay plot comprising all cell subsets used in the analysis (see also figure 1B-D). (B) Frequency of major cell types within specified patient tumors. Colors and labels denote the major cell subsets. (C) Frequency of cells in each major cell type within control (blue) and SBRT-treated (red) patient samples. Statistical significance was calculated using multiple unpaired t-tests (*p < 0.05). Data presented as mean ± standard deviation.



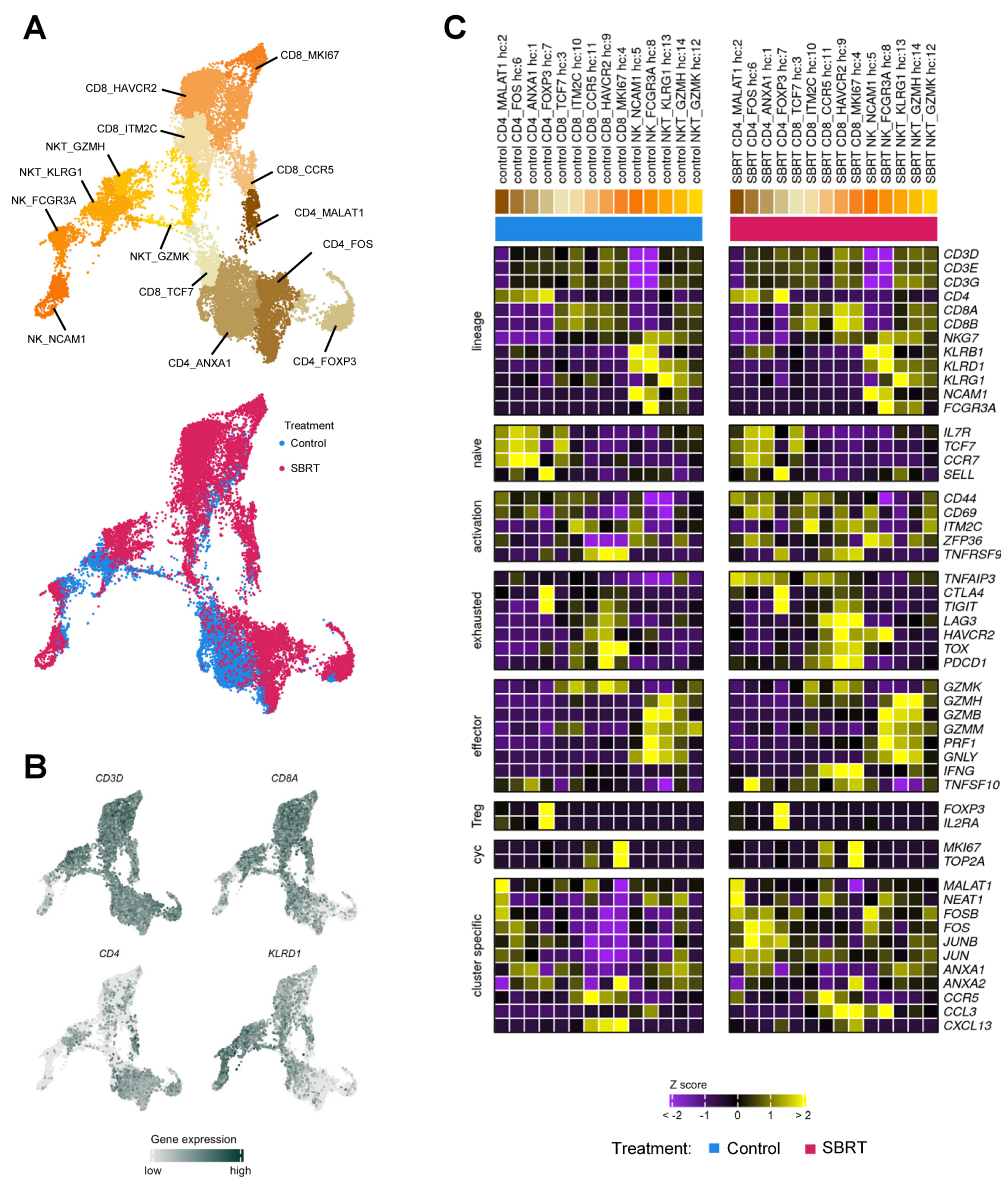
Supplemental Figure 2. Analysis of CD8⁺ T cells by spectral flow cytometry. (A) Gating strategy to export out CD8⁺ T cells from each patient sample for further analysis. (B) t-SNE overlay plot for CD8⁺ T cells used in the analysis. (C) Individual t-SNE plots for indicated samples. (D) Frequency of CD8⁺ T cell clusters within specified patient tumors. Colors and labels indicate the fifteen identified clusters by FlowSOM hierarchical clustering (see also figure 2A). (E) Heatmap showing expression of markers used for generating FlowSOM clusters and t-SNE plots for CD8⁺ T cells in all identified clusters.



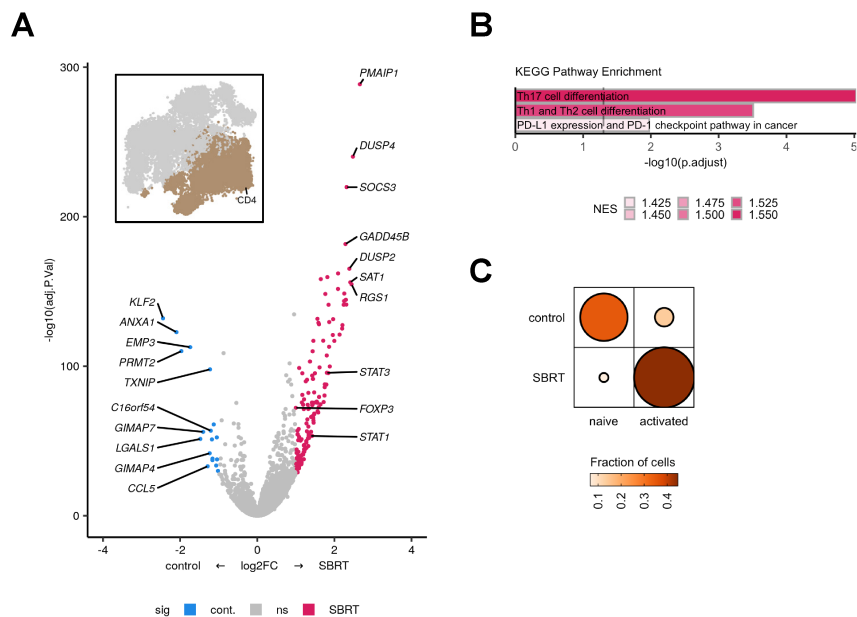
Supplemental Figure 3. Histogram analysis of all CD8⁺ T cell clusters identified by FlowSOM. Single parameter histograms are shown for comparison across 15 clusters identified by FlowSOM analysis. Numbers indicate median fluorescent intensity (MFI) value. Histogram for cumulative expression of listed markers in all CD8⁺ T cells is also included (CI 1-15).



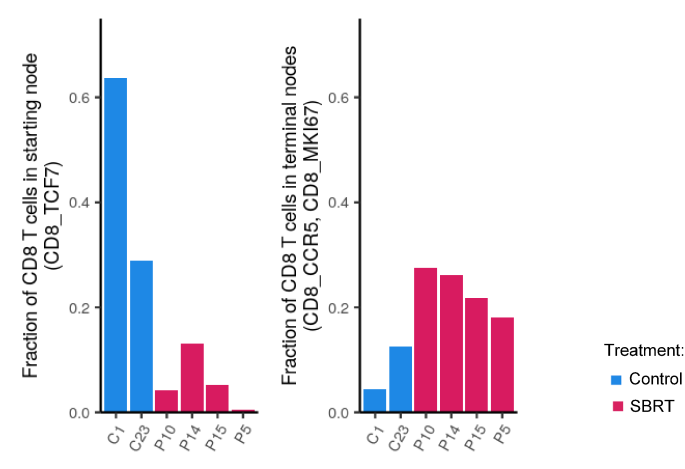
Supplemental Figure 4. Distribution of cells within cell classes and treatment groups. (A) Left, scRNAseq data of all cells plotted by treatment group (see also figure 3A). Right, overall number and distribution by treatment group of cells within broad cell classes. (B) Overall number and distribution by broad cell class within treatment groups. (C) Localized gene expression for indicated genes within the t-SNE. (D) Heatmap showing expression of established lineage markers by broad cell class. (E) Left: Expression of indicated genes by main class. Y axis is log counts. Red dash is mean expression. For each plot, $p < 2.2e-16$ by ANOVA. Right: Gene expression plotted on parent t-SNE.



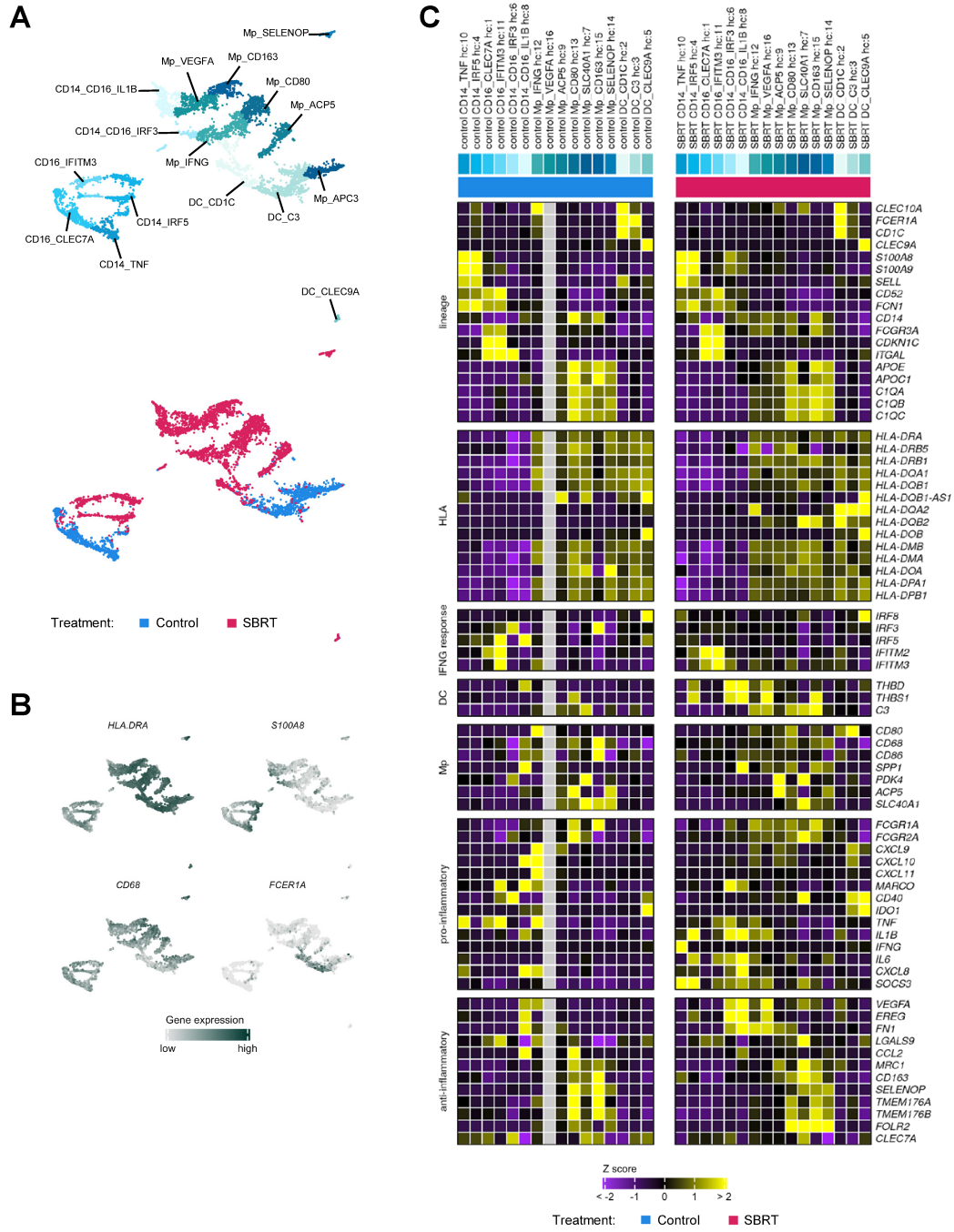
Supplemental Figure 5. Subclassification of lymphocytes. (A) UMAP recalculated for lymphocytes subset from the parent data. Top, lymphocyte reclustering into 14 subclusters. Bottom, distribution of cells by treatment group. (B) Localized gene expression for indicated genes within the lymphocyte UMAP. (C) Heatmaps showing expression of genes used for lymphocyte subclassification, divided by treatment group.



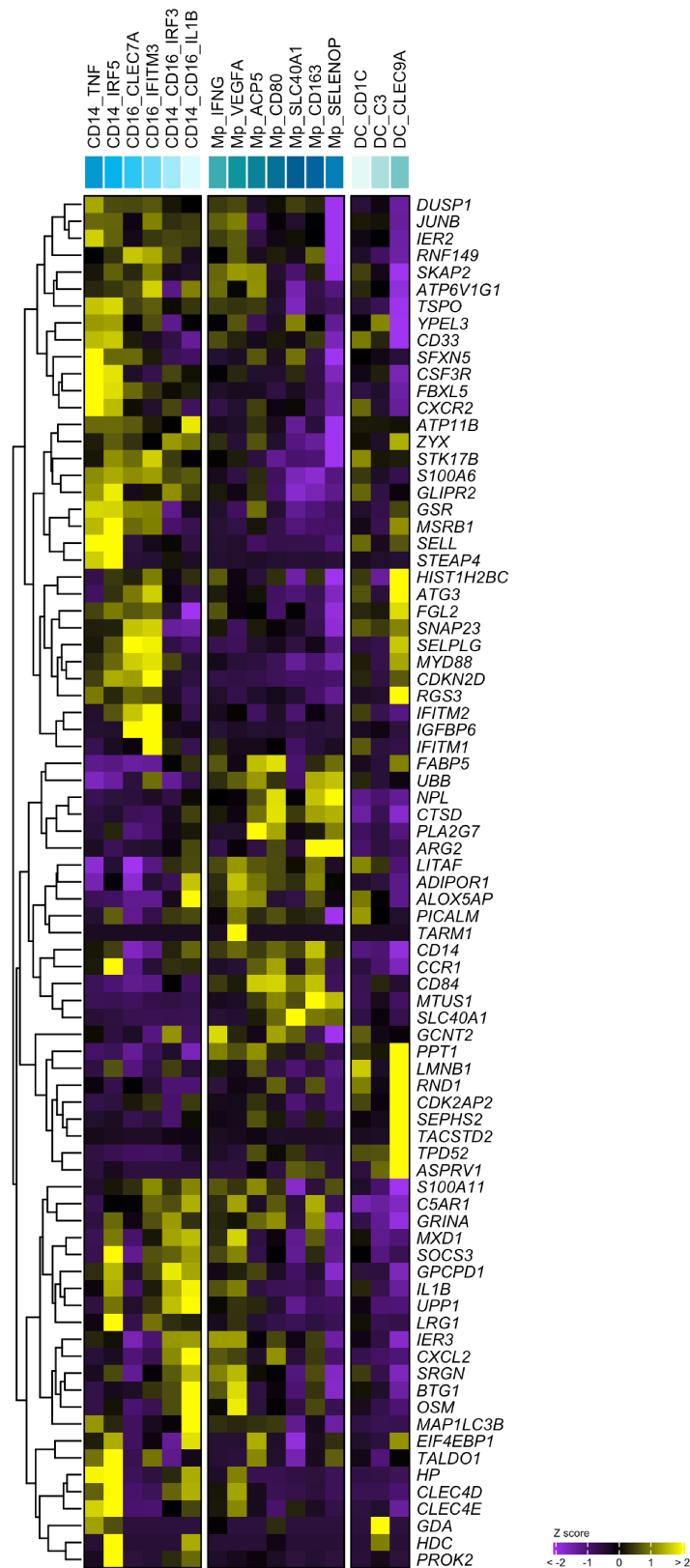
Supplemental Figure 6. Analysis of CD4⁺ T cells. (A) Volcano plot showing DGE within CD4⁺ T cells between treatment groups. Color is differential gene expression, $abs(log_2FC) > 1$; $adj.p < 0.05$. Inset, CD4⁺ T cells subset from lymphocyte t-SNE. (B) GSEA of KEGG pathways. Opacity is NES. All shown pathways are significant, $p.adjust < 0.05$. (C) Visualized chi square of naive CD4⁺ T cells versus treatment group. Size and color show relative abundance after controlling for different total CD4⁺ T cell numbers between treatment groups.



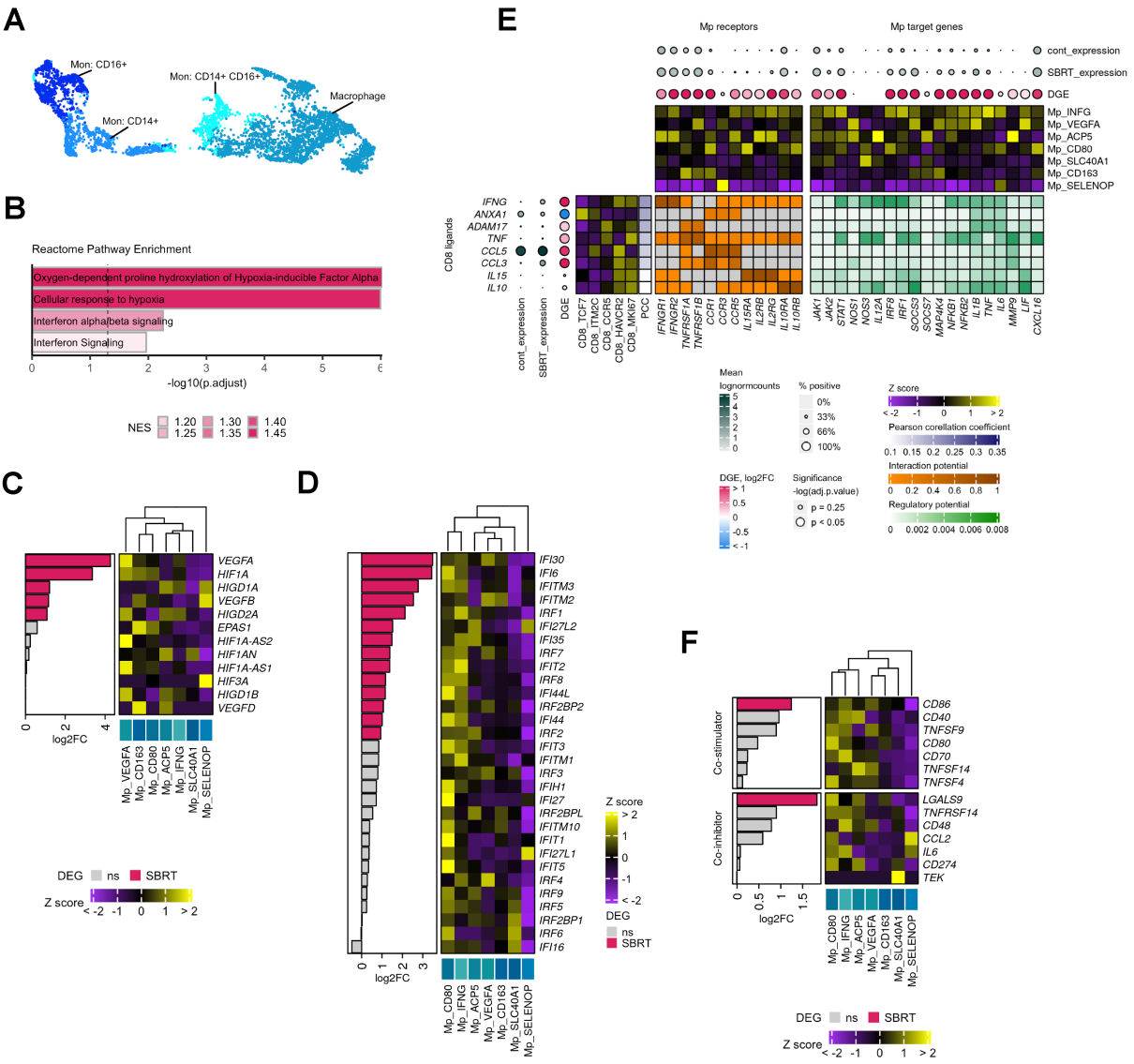
Supplemental Figure 7. Analysis of CD8⁺ T cell maturation across individual patient samples. Bar chart showing the fraction of CD8⁺ T cells in the pseudotime starting node (CD8_TCF7 dense) or pooled terminal nodes (CD8_MKI67, CD8_CCR5) for each patient. Color is treatment group for the sample.



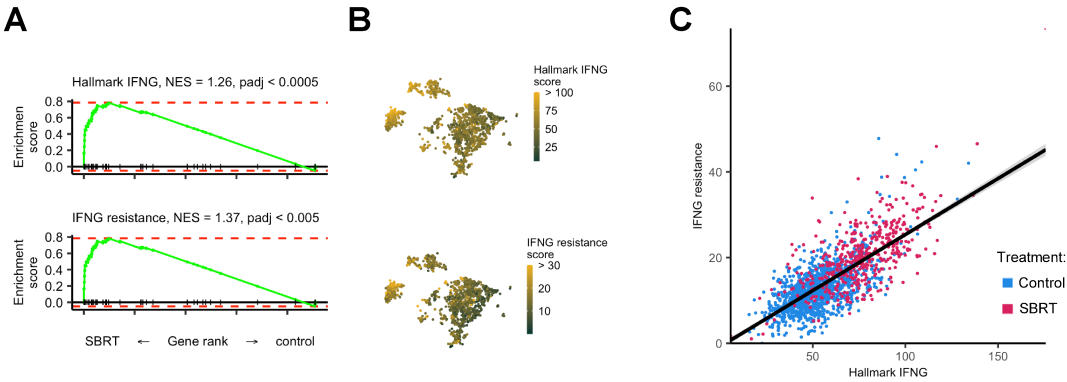
Supplemental Figure 8. Subclassification of myeloid cells. (A) UMAP recalculated for myeloid cells subset from the parent data. Top, myeloid cells reclustering into 16 subclusters. Bottom, distribution of cells by treatment group. (B) Localized gene expression for indicated genes within the myeloid UMAP. (C) Heatmaps showing expression of genes used for myeloid subclassification, divided by treatment group. Grey is no cells in the indicated subclass.



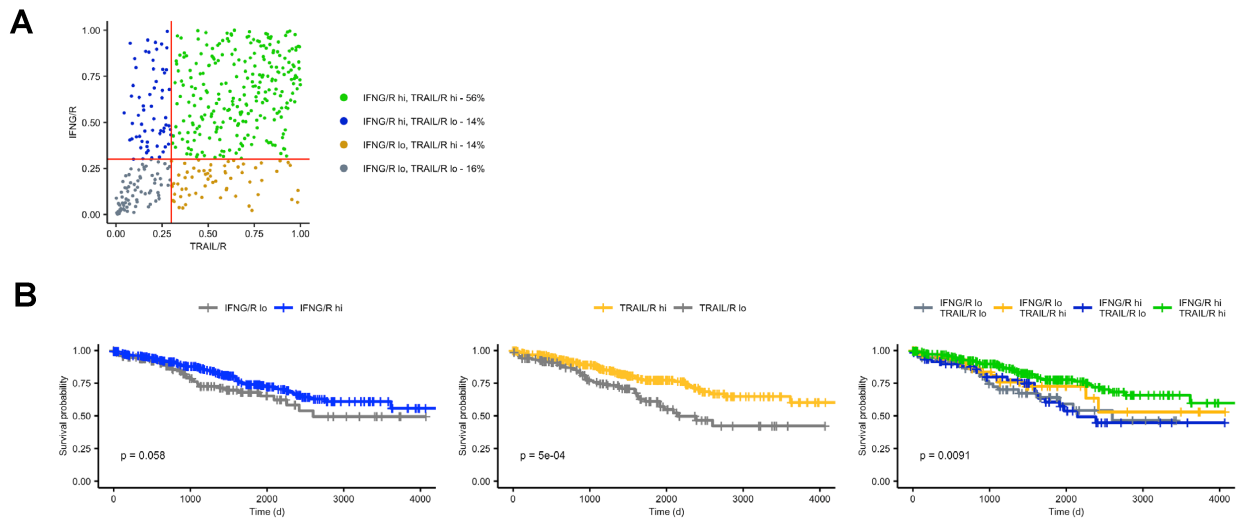
Supplemental Figure 9. MDSC gene signature in myeloid subclasses. Heatmap showing expression of MDSC signature genes across all identified myeloid subclasses.



Supplemental Figure 10. Analysis of macrophage subclasses. (A) Macrophages subset from monocyte and macrophage parent data. (B) GSEA of Reactome pathways. Opacity is NES. All shown pathways are significant, p.adj < 0.05. (C) Heatmap showing expression of indicated hypoxia associated genes by macrophage subclasses. Columns are clustered by gene expression. Bar graph shows log2FC by treatment group. Color is differential gene expression, log2FC > 1; p.adj < 0.05. (D) Heatmap showing expression of indicated interferon response genes by macrophage subclasses. Columns are clustered by gene expression. Bar graph shows log2FC by treatment group. Color is differential gene expression, log2FC > 1; p.adj < 0.05. (E) Predicted interactions from CD8 ligands to macrophage receptors and target genes. CD8 ligands are ordered by decreasing correlation to target gene expression, PCC. Z score and DGE are calculated separately for either the CD8+ T cells or macrophage subsets. (F) Heatmap showing expression of indicated co-stimulatory and co-inhibitory genes by macrophage subclasses. Columns are clustered by gene expression. Bar graph shows log2FC by treatment group. Color is differential gene expression, log2FC > 1; p.adj < 0.05.



Supplemental Figure 11. Analysis of hallmark IFNG and IFNG resistance gene signatures in tumor cells. (A) GSEA of hallmark IFNG response and IFNG resistance pathways.³⁶ (B) Localization of hallmark IFNG and resistance signal by tumor cell t-SNE coordinates. (C) Dot plot showing hallmark IFNG response score versus IFNG resistance score with linear regression. Color is treatment group.



Supplemental Figure 12. Analysis of potential IFNG and TRAIL ligand to receptor interactions for RCC patient survival and ICB treatment response. Figure S12A-B analyze TCGA-KIRC primary tumors for stages I-III. (A) Dot plot showing distribution of TCGA patient tumors by TRAIL/IFNG receptor and IFNG/IFNG receptor. Red lines show thresholds from hi and lo designations. Color is classification. (B) Kaplan-Meier curves comparing cross sections of samples from Figure S12A. Left: IFNG/R hi vs. low (right vs. left of vertical line); hazard ratio of IFNG/R hi = 0.68. Middle: TRAIL/R hi vs. low (above vs. below horizontal line); hazard ratio of TRAIL/R hi = 0.54. Right: Mixed effect model of IFNG/R score + TRAIL/R score; hazard ratio of IFNG/R hi = 0.8; hazard ratio of TRAIL/R hi = 0.57.

Patient	Treatment	Sex	Age	Path (T) Stage	Histology	scRNA Seq	Spectral Flow Cytometry
C1	Control	F	79	1B	Clear Cell	x	
C3	Control	F	53	1B	Clear Cell		x
C4	Control	M	63	3A	Clear Cell		x
C5	Control	F	61	1B	Clear Cell		x
C6	Control	M	55	2B	Clear Cell		x
C7	Control	M	53	3	Clear Cell		x
C8	Control	M	70	1B	Clear Cell		x
C23	Control	M	67	1B	Clear Cell	x	
P1	SBRT	M	53	2A	Clear Cell		x
P5	SBRT	M	67	3A	Clear Cell	x	x
P7	SBRT	M	67	3A	Clear Cell		x
P10	SBRT	F	75	3A	Clear Cell	x	
P14	SBRT	M	62	3A	Clear Cell	x	x
P15	SBRT	F	57	2A	Clear Cell	x	x

Supplemental Table 1. Patient demographic and clinical characteristics.
List of patients, their treatment method, demographics (sex and age), pathology, histology, and the method of analysis.

Sl. No.	Marker	Clone	Fluorochrome	Dilution	Supplier	Catalog#
1	CCR5	2D7	BUV395	1 in 50	BD	565224
2	Live/Dead		LIVE/DEAD™ Blue	1 in 500	ThermoFisher	L34962
3	CD31	L1331.1	BUV496	1 in 200	BD	749833
4	CD14	MφP9	BUV563	1 in 100	BD	741441
5	CD261	S35-934	BUV615	1 in 50	BD	752308
6	CD11c	B-ly6	BUV661	1 in 200	BD	612967
7	CD56	NCAM16.2	BUV737	1 in 200	BD	612766
8	CD45RO	UCHL1	BUV805	1 in 100	BD	748367
9	CD68	Y1/82A	BV421	1 in 50	BD	564943
10	CD27	O323	SB436	1 in 200	ThermoFisher	62-0279-42
11	CD8	SK1	Pacific Blue	1 in 200	Biolegend	980906
12	KI67	B56	BV480	1 in 50	BD	566109
13	CD204	U23-56	BV510	1 in 50	BD	742439
14	CD4	RPA-T4	Pacific Orange	1 in 100	ThermoFisher	79-0049-42
15	CD28	CD28.2	BV605	1 in 100	Biolegend	302967
16	CXCR3	G025H7	BV650	1 in 50	Biolegend	353729
17	CCR6	G034E3	BV711	1 in 100	Biolegend	353435
18	CCR4	1G1	BV750	1 in 50	BD	746980
19	CCR7	G043H7	BV785	1 in 50	Biolegend	353229
20	CD57	NK-1	FITC	1 in 200	BD	555619
21	CD3	SK-7	Spark Blue 550	1 in 100	Biolegend	344852
22	CD45	2D1	Nova Blue 610	1 in 100	ThermoFisher	H005T03B05
23	PD-1	EH12.1	PerCP-Cy5.5	1 in 50	BD	561273
24	LAG3	3DS223H	PerCP-eFluor710	1 in 50	ThermoFisher	46-2239-42
25	TOX	REA473	PE	1 in 50	Miltenyi	130-120-716
26	TIGIT	A15153G	PE/Dazzle 594	1 in 50	Biolegend	372716
27	CD25	M-A251	PE-Fire/640	1 in 50	Biolegend	356148
28	CD33	HIM3-4	PE-Cy5	1 in 100	ThermoFisher	15-0339-42
29	CD127	A019D5	PE-Fire 700	1 in 100	Biolegend	351366
30	CD253	RIK-2	PE Cy7	1 in 50	Biolegend	308216
31	TIM3	F38-2E2	APC	1 in 50	ThermoFisher	62-3109-42
32	CD45RA	HI100	Spark NIR 685	1 in 200	Biolegend	304168
33	CX3CR1	G025H7	R718	1 in 50	Biolegend	353730
34	CD38	HIT2	APC-eFluor780	1 in 200	ThermoFisher	47-0389-42
35	HLA-DR	L243	APC/Fire 810	1 in 100	Biolegend	307674

Supplemental Table 2. Antibody panel details. List of antibodies, clones, fluorochromes, dilutions, manufacturer, and catalog numbers used in spectral flow cytometry analysis.

Patients	Cluster frequencies of major cell subsets in each patient					
	CD8 ⁺	CD4 ⁺	T-reg	Myeloid	NK	CD45 ⁺
C3	50.3%	20.2%	2.9%	8.9%	15.7%	2.0%
C4	18.1%	16.5%	2.8%	41.7%	17.3%	3.5%
C5	18.6%	16.0%	2.6%	14.9%	20.2%	27.6%
C6	26.2%	6.0%	0.3%	32.3%	15.2%	20.0%
C7	19.3%	18.5%	2.6%	30.2%	22.0%	7.3%
C8	18.8%	16.5%	1.0%	47.7%	5.9%	10.1%
P1	16.8%	13.9%	1.1%	31.2%	10.5%	26.5%
P5	65.0%	12.6%	3.0%	9.7%	2.0%	7.8%
P7	19.4%	24.2%	2.6%	11.5%	6.1%	36.4%
P14	26.8%	22.2%	5.3%	14.3%	13.6%	17.8%
P15	6.9%	9.9%	0.7%	6.9%	1.7%	74.0%

0

100

Cluster Frequency (%)

Supplemental Table 3. Cluster frequencies from spectral flow cytometry analysis. Cluster frequencies for major cell subsets identified by spectral flow cytometry analysis in six control (C3, C4, C5, C6, C7, and C8) and five SBRT treated (P1, P5, P7, P14, and P15) patient samples.

Patient	Cluster frequencies for CD8 ⁺ T cells in each cluster identified by FlowSOM														
	1	2	3	4	5	6	7	8	9	10	11	12	13	14	15
C3	5.09%	7.16%	0.48%	0.79%	1.85%	2.71%	1.66%	7.99%	2.33%	1.50%	13.63%	3.37%	27.94%	11.32%	12.17%
C4	0.90%	0.82%	0.16%	0.08%	2.19%	0.89%	1.71%	9.99%	2.38%	0.93%	9.90%	1.60%	57.43%	6.95%	4.05%
C5	1.52%	1.55%	0.10%	0.34%	0.97%	3.36%	0.66%	25.36%	1.82%	1.91%	30.30%	0.79%	10.17%	2.29%	18.84%
C6	2.02%	13.00%	4.57%	30.94%	17.37%	1.49%	0.84%	3.64%	13.17%	2.63%	3.24%	0.79%	3.87%	0.86%	1.58%
C7	9.16%	1.81%	0.49%	7.05%	1.15%	9.44%	1.37%	11.10%	3.80%	1.75%	8.69%	1.02%	35.17%	4.34%	3.66%
C8	38.54%	16.42%	1.12%	5.10%	3.30%	3.01%	0.67%	3.61%	3.80%	4.04%	9.81%	1.13%	6.41%	0.66%	2.37%
P1	3.85%	12.28%	2.09%	3.14%	2.27%	2.15%	1.15%	8.18%	3.01%	2.62%	8.39%	2.06%	24.30%	11.20%	13.32%
P5	1.59%	3.79%	2.69%	1.38%	3.38%	0.23%	0.32%	1.21%	0.33%	2.10%	2.91%	10.85%	8.85%	8.14%	52.21%
P7	4.71%	1.63%	2.33%	5.28%	2.44%	1.85%	12.39%	12.08%	2.27%	1.34%	5.06%	2.31%	12.63%	21.45%	12.23%
P14	9.97%	5.77%	5.73%	0.51%	3.80%	0.89%	2.77%	7.97%	1.43%	2.72%	6.55%	7.90%	6.68%	11.68%	25.62%
P15	3.16%	8.13%	4.41%	5.52%	5.42%	2.54%	7.43%	6.26%	1.29%	2.30%	9.60%	4.46%	8.25%	8.44%	22.79%

0

100

Cluster Frequency (%)

Supplemental Table 4. Cluster frequencies of CD8⁺ T cells from spectral flow cytometry analysis. Cluster frequencies for CD8⁺ T cell clusters identified by spectral flow cytometry analysis in six control (C3, C4, C5, C6, C7, and C8) and five SBRT treated (P1, P5, P7, P14, and P15) samples.

Sub class	Raw cell numbers					
	C1	C23	P10	P14	P15	P5
CD4_ANXA1	3170	165	188	37	233	177
CD4_FOS	157	654	430	576	746	704
CD4_FOXP3	241	88	328	384	160	462
CD4_MALAT1	161	6	179	91	96	89
CD8_CCR5	25	6	84	112	67	338
CD8_HAVCR2	202	178	252	463	150	3315
CD8_ITM2C	164	46	142	179	182	958
CD8_MKI67	26	42	76	165	32	604
CD8_TCF7	728	111	25	140	24	27
NK_FCGR3A	202	545	77	158	47	37
NK_NCAM1	302	92	235	377	62	93
NKT_GZMH	5	10	74	107	197	450
NKT_GZMK	49	145	101	434	56	65
NKT_KLRG1	58	1223	58	396	164	29

Supplemental Table 5. Single-cell RNA sample composition. Raw cell numbers for distinct T and NK cell subclasses identified in control (C1 and C23) and SBRT treated (P10, P14, P15, and P5) patients by single-cell RNA seq analysis.

Supplemental methods

Section I: MIFlowCyt Document

Section II: Cell Interaction Analysis

Section I: MIFlowCyt Document

1. Experiment Overview

1.1. Purpose: The goal of these studies was to evaluate lymphoid populations within renal cell carcinoma (RCC) patient tumors following radiation treatment as previously described (Singh et al. Clinical Cancer Research, 2017). Based on the findings of increased clonality of T cells in irradiated RCC (Chow et al. PNAS, 2020), we hypothesized that radiation increases levels of activated and proliferating CD8⁺ T cells in tumor microenvironment.

1.2. Keywords: Renal Cell Carcinoma, High-dimensional flow cytometry, Lymphocytes, Radiation

1.3. Experiment Variables: Six nephrectomy only (control) RCC patient tumor samples were compared to five radiation treated patient tumors (nephrectomy four weeks post radiation).

1.4. Organization:

- 1.4.1. Name:** Roswell Park Comprehensive Cancer Center
- 1.4.2. Address:** Roswell Park Comprehensive Cancer Center, Elm and Carlton Streets, Buffalo, NY, 14263

1.5. Primary Contact:

- 1.5.1. Name:** Jason Muhitch
- 1.5.2. Email Address:** jason.muhitch@roswellpark.org

1.6. Date: The first tumor sample was collected on July 11, 2013. Final analysis of spectral flow cytometry CD8 data was completed in February 2023.

1.7. Conclusions: We identified increased levels of four distinct T cell populations in RCC patient tumor that had been treated with radiation therapy. Two of these populations showed increased levels of markers for exhaustion and proliferation.

1.8. Quality Control Measures: Antibodies used in the assay were titrated and saturating concentrations were used. Pilot experiments were performed prior to the main assay to validate the functionality of the all the antibodies in the panel using PBMCs and tumor samples. The Cytex Aurora instrument was QC daily using SpectraFlo® QC Beads (Cytex; Cat #N7-97355) to adjust laser performance based on baseline settings, laser delay, and to align height and area scaling factors for optimal signal resolution to ensure consistent performance was achieved daily.

2. Flow Sample/Specimen Details

2.1. Sample/Specimen Material Description : Renal cell carcinoma patient tumors with or without

radiation treatment were resected, processed to single cell suspension, and cryopreserved. Preserved samples were thawed and used for flow cytometry analysis. Sample source, patient age, gender, phenotype, and treatment

SI No	Sample Description	Source	Organism	Age	Gender	Phenotype Tumor Grade	Treatment
1	Single cell suspension	ccRCC tumors	Homo sapiens	53	F	3	None
2	Single cell suspension	ccRCC tumors	Homo sapiens	63	M	3A	None
3	Single cell suspension	ccRCC tumors	Homo sapiens	61	F	1B	None
4	Single cell suspension	ccRCC tumors	Homo sapiens	55	M	2B	None
5	Single cell suspension	ccRCC tumors	Homo sapiens	53	M	3	None
6	Single cell suspension	ccRCC tumors	Homo sapiens	70	M	1B	None
7	Single cell suspension	ccRCC tumors	Homo sapiens	53	M	2A	15Gy Radiation
8	Single cell suspension	ccRCC tumors	Homo sapiens	67	M	3A	15Gy Radiation
9	Single cell suspension	ccRCC tumors	Homo sapiens	67	M	3A	15Gy Radiation
10	Single cell suspension	ccRCC tumors	Homo sapiens	62	M	3A	15Gy Radiation
11	Single cell suspension	ccRCC tumors	Homo sapiens	57	F	2A	15Gy Radiation

ccRCC: clear cell Renal Cell Carcinoma

are described in the table.

2.2. Sample Characteristics: Renal cell carcinoma tumors are heavily infiltrated by immune cells. Evaluation of patient RCC tumors by mass cytometry has shown large cohorts of lymphocytes and myeloid populations.

2.3. Sample Treatment(s) Description: Patients received radiation dose (15Gy) as previously described (Singh et al. Clinical Cancer Research, 2017). Tumors were resected 4 weeks post radiation and processed to single cell suspension via enzymatic digestion prior to cryopreservation as previously described (Chow et al. PNAS, 2020). Single cell suspensions from non-irradiated patient tumors were used as controls.

2.4. Fluorescence Reagent(s) Description: Fluorescent reagent information (characteristic being measured, analyte, analyte detector, analyte reporter, clone, manufacturer, catalog number and dilution used) is described in the table.

SI No	Characteristic being measured	Analyte	Analyte detector (antibody)	Analyte reporter (fluorochrome)	Clone	Supplier	Catalog	Dilution
1	Cell surface protein	CCR5	Anti-CCR5	BUV395	2D7	BD	565224	1 in 50
2	Cell surface protein	Live/Dead	L/D Blue Stain	LIVE/DEAD™ Blue		ThermoFisher	L34962	1 in 500
3	Cell surface protein	CD31	Anti-CD31	BUV496	L1331.1	BD	749833	1 in 200
4	Cell surface protein	CD14	Anti-CD14	BUV563	MφP9	BD	741441	1 in 100
5	Cell surface protein	CD261	Anti-CD261	BUV615	S35-934	BD	752308	1 in 50
6	Cell surface protein	CD11c	Anti-CD11c	BUV661	B-ly6	BD	612967	1 in 200
7	Cell surface protein	CD56	Anti-CD56	BUV737	NCAM16.2	BD	612766	1 in 200
8	Cell surface protein	CD45RO	Anti-CD45RO	BUV805	UCHL1	BD	748367	1 in 100
9	Intracellular protein	CD68	Anti-CD68	BV421	Y1/82A	BD	564943	1 in 50
10	Cell surface protein	CD27	Anti-CD27	SB436	O323	ThermoFisher	62-0279-42	1 in 200
11	Cell surface protein	CD8	Anti-CD8	Pacific Blue	SK1	Biolegend	980906	1 in 200
12	Intracellular protein	KI67	Anti-KI67	BV480	B56	BD	566109	1 in 50
13	Cell surface protein	CD204	Anti-CD204	BV510	U23-56	BD	742439	1 in 50
14	Cell surface protein	CD4	Anti-CD4	Pacific Orange	RPA-T4	ThermoFisher	79-0049-42	1 in 100
15	Cell surface protein	CD28	Anti-CD28	BV605	CD28.2	Biolegend	302967	1 in 100
16	Cell surface protein	CXCR3	Anti-CXCR3	BV650	G025H7	Biolegend	353729	1 in 50
17	Cell surface protein	CCR6	Anti-CCR6	BV711	G034E3	Biolegend	353435	1 in 100
18	Cell surface protein	CCR4	Anti-CCR4	BV750	1G1	BD	746980	1 in 50
19	Cell surface protein	CCR7	Anti-CCR7	BV785	G043H7	Biolegend	353229	1 in 50
20	Cell surface protein	CD57	Anti-CD57	FITC	NK-1	BD	555619	1 in 200
21	Cell surface protein	CD3	Anti-CD3	Spark Blue 550	SK-7	Biolegend	344852	1 in 100
22	Cell surface protein	CD45	Anti-CD45	Nova Blue 610	2D1	ThermoFisher	H005T03B05	1 in 100
23	Cell surface protein	PD1	Anti-PD1	PerCP-Cy5.5	EH12.1	BD	561273	1 in 50
24	Cell surface protein	LAG3	Anti-LAG3	PerCP-eFluor710	3DS223H	ThermoFisher	46-2239-42	1 in 50
25	Intracellular protein	TOX	Anti-TOX	PE	REA473	Miltenyi	130-120-716	1 in 50
26	Cell surface protein	TIGIT	Anti-TIGIT	PE/Dazzle 594	A15153G	Biolegend	372716	1 in 50
27	Cell surface protein	CD25	Anti-CD25	PE-Fire/640	M-A251	Biolegend	356148	1 in 50
28	Cell surface protein	CD33	Anti-CD33	PE-Cy5	HIM3-4	ThermoFisher	15-0339-42	1 in 100
29	Cell surface protein	CD127	Anti-CD127	PE-Fire 700	A019D5	Biolegend	351366	1 in 100
30	Cell surface protein	CD253	Anti-CD253	PE Cy7	RIK-2	Biolegend	308216	1 in 50
31	Cell surface protein	TIM3	Anti-TIM3	APC	F38-2E2	ThermoFisher	62-3109-42	1 in 50
32	Cell surface protein	CD45RA	Anti-CD45RA	Spark NIR 685	HI100	Biolegend	304168	1 in 200
33	Cell surface protein	CX3CR1	Anti-CX3CR1	R718	G025H7	Biolegend	353730	1 in 50
34	Cell surface protein	CD38	Anti-CD38	APC-eFluor780	HIT2	ThermoFisher	47-0389-42	1 in 200
35	Cell surface protein	HLA-DR	Anti-HLADR	APC/Fire 810	L243	Biolegend	307674	1 in 100

3. Instrument Details

3.1. Instrument Manufacturer: Cytex Biosciences

3.2. Instrument Model: Cytex™ Aurora

3.3.1. Instrument Configuration and Settings:

3.3.1.1. Flow cells: Clean Flow Cell, 12x75 mm polystyrene and polypropylene tubes

3.3.1.2. Fluidics Information: Sample flow rates – Low (15µL/min), Medium (30µL/min), High (60µL/min).

3.3.2. Light Source(s)

3.3.2.1. Light source type: Lasers

3.3.2.2. Light source excitatory wavelength: 335 nm, 405 nm, 488 nm, 561 nm, 640 nm

3.3.2.3. Light source power at excitatory wavelength: 335 nm (20 mW), 405 nm (100 mW), 488 nm (50 mW), 561 nm (50 mW), 640 nm (80 mW)

3.3.2.4. Light source beam: Flat-Top laser beam profile with narrow vertical beam height optimized for small particle detection.

3.3.3. Excitation optics configuration:

Ultraviolet detector module: 16 channels unevenly spaced bandwidth from 365-829 nm.

Violet detector module: 16 channels unevenly spaced bandwidth from 420-829 nm.

Blue detector module: 14 channels unevenly spaced bandwidth from 498-829 nm.

Yellow-Green detector module: 10 channels unevenly spaced bandwidth from 567-829 nm.

Red detector module: 8 channels unevenly spaced bandwidth from 652-829 nm.

3.3.4. Optical Filters:

FSC: high-performance semiconductor detector with 488nm bandpass filter

SSC: two high-performance semiconductor detectors with 405nm and 488nm bandpass filters

3.3.5. Optical detectors: Proprietary high sensitivity Coarse Wavelength Division Multiplexing (CWDM) semiconductor array per laser.

3.4 Other Information:

POWER: 100-140 VAC, 15A or 200-250 VAC, 10A

HEAT DISSIPATION: 500 W with all solid-state lasers

TEMPERATURE: 15–28°C

HUMIDITY: 20%-85% relative non-condensing

AIR FILTERING: No excessive dust or smoke

LIGHTING: No special requirements

4. Data Analysis Details

4.1. List-mode Data File: Both Raw and Unmixed FCS files for 11 patients will be available for download at ImmPort under access code SDY1998 post acceptance.

4.2. Compensation Details: Live spectral unmixing was performed using SPECTROFLO SOFTWARE during sample acquisition. A second compensation step was performed using FCS Express 7. Compensation matrix is provided with the FCS datafiles.

4.3. Data Transformation Details:

4.3.1. Purpose of Data Transformation: FlowSOM clustering was used to performed unsupervised clustering for the purpose of identifying subsets within CD8+ cells. tSNE analysis (dimensionality reduction) was done to visualize these clusters on a 2D plot. Both analyses were performed using the pipeline feature of FCS Express 7.

4.3.2. Data Transformation Description: The steps used in the pipeline are described below.

FlowSOM: To identify CD8+ subsets, all CD8+ cells from each unmixed patient data files were first exported out as new FCS files. Gating strategy is highlighted in supplementary figure 2a. 10000 events from each CD8+ data files were then concatenated (using FCS Express) to generate one FCS file with all patient data combined. This file was then used to perform FlowSOM and tSNE analyses.

FlowSOM hierarchical clustering to identify subpopulations was performed using CCR4, CCR5, CCR6, CCR7, CD25, CD27, CD28, CD38, CD45-RA, CD45-RO, CD56, CD57, CD127, CXCR3, CX3CR1, HLA-DR, KI67, LAG3, PD-1, TIGIT, TIM3, and TOX markers.

New Scaling: The specified parameters were scaled using the new scaling step. Additional 0-1 scaling step was performed to visualize the data on one scale.

Batch Self-Organizing Map: 0 to 1 scaled parameter for each marker were used to run the batch self-organizing map step. The following settings were used:

Transformation Options

☒ Add Meta-Clustering as New Parameter

☒ Add Meta-Clustering To Selected Parameter

Coarse Training Options

Number of Cycles

20

Neighborhood Spread: Initial

3

Final

0.5

Fine-Tune Training Options

Number of Cycles

10

Neighborhood Spread: Initial

0.5

Final

0.5

☒ Automatic Neighborhood Spread

SOM 2D Grid:

Width

10

Height

10

New Parameter Name

Batch SOM Cluster Assignm

Cluster Centroids Initialization Method

☐ Random

☒ Random Cells

Training Decay Function

☐ Asymptotic

☒ Linear

2D Grid Neighborhood Function

☒ Gaussian

☐ Boxcar

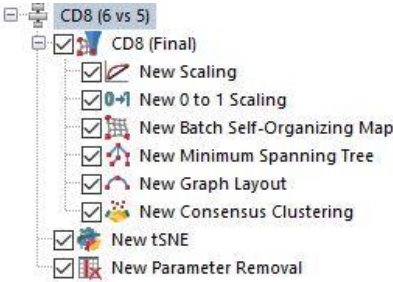
2D Grid Distance Metric

☒ Euclidean (L2-norm)

☐ Chebyshev (Linf-norm)

Generate New Random Seed

6



Minimum spanning tree and **Graph Layout** were generated with default software set up.

Consensus clustering was performed with following settings:

Transformation Options	
<input checked="" type="checkbox"/>	Add Meta-Clustering as New Parameter
<input checked="" type="checkbox"/>	Add Meta-Clustering To Selected Parameter
Number of Clusters	15
Sampling Fraction	0.9
Number of Samplings	100
New Parameter Name	Consensus Clustering Assignments
Clustering Algorithms	
<input type="radio"/>	KMeans
<input checked="" type="radio"/>	Hierarchical
Generate New Random Seed	6

tSNE: 0 to 1 scaled **values** of specified parameters were used to generate tSNE plots. Following settings were used to generate the plots:

Transformation Options	
Suffix for transformed parameters	
tSNE Method To Use	
<input type="radio"/>	Exact tSNE
<input checked="" type="radio"/>	Barnes-Hut Approximation
Amount of Approximation (Applies only to Barnes-Hut)	0.50
Perplexity	50
Number of Iterations	5000
<input type="checkbox"/>	Use Opt-SNE
Generate New Random Seed	6

4.3.3. Other relevant data: All spectral analyses was performed using FCS Express7 software package (De 517 Novo Software, version 7.08.0018)

4.4. Gating (Data Filtering) Details:

4.4.1. Gate Description: Gating strategy to export out CD8⁺ T cell events from all patient files is shown in supplemental figure 2a.

4.4.2. Gate Statistics: Frequencies for each sub-cluster for each patient is highlighted in supplemental table 4.

4.4.3. Gate Boundaries: Gates for different clusters on tSNE plots were generated using consensus clustering assignments identified via FlowSOM.

Section II: Cell interaction analysis

Relevant target cell genes for responses of interest were identified from established pathways and relevant publications (KEGG 04612, Antigen processing and presentation; KEGG 04210, Apoptosis; KEGG 05140, Leishmaniasis; Dror et al. 2007)³⁵; second, potential ligands from source cells were identified by a ranked by Pearson correlation calculated based on cross referencing top-expressed source cell genes with a ligand-target-matrix²⁰; potential target cell receptors were identified by cross-referencing top-expressed target cell genes with a ligand-receptor-network²⁰ of established physical interactors of predicted source cell ligands.